

## Supporting information

# **Rigid two-dimensional indium metal-organic frameworks boosting nitrogen electroreduction at all pH values**

Yuntong Sun, Baokai Xia, Shan Ding, Licheng Yu, Sheng Chen,\* Jingjing Duan\*

Key Laboratory for Soft Chemistry and Functional Materials (Ministry of Education), School of Chemical Engineering, School of Energy and Power Engineering, Nanjing University of Science and Technology, Nanjing, 210094, China

Correspondence and requests for materials should be addressed to [sheng.chen@njust.edu.cn](mailto:sheng.chen@njust.edu.cn);

[jingjing.duan@njust.edu.cn](mailto:jingjing.duan@njust.edu.cn)

## Supplementary Methods

### I. Experimental section

#### 1. Material synthesis

**1.1. Synthesis of 2D In-MOF nanosheets.** 100 mg 2,5-thiophenedicarboxylic acid ( $C_6H_4O_4S$ , TDC) was dissolved in 10 mL ethanol solution, which was then mixed with 20 mL ethanol solution containing of 50 mg indium chloride tetrahydrate ( $InCl_3 \cdot 4H_2O$ ) and 50 mg cadmium acetate  $Cd(Ac)_2 \cdot 3H_2O$ . The mixture was heated at 60 °C for 12 hours (hrs). The as-obtained product was collected, and washed with copious ethanol and water, respectively.

To test its rigidity property at all pH values, the as-synthesized 2D In-MOF was then soaked in different aqueous solutions for 24 hrs, for example, 0.05 M  $H_2SO_4$  (pH =1), 0.1 M  $Na_2SO_4$  (pH =7), and 1 M KOH (pH = 14). The solutions with other pH values were prepared by mixing desirable amounts of 0.1 M  $Na_2SO_4$  and 0.05 M  $H_2SO_4$  or 1 M KOH solutions.

**1.2. Synthesis of bulk In-MOF.** 100 mg 2,5-thiophenedicarboxylic acid ( $C_6H_4O_4S$ , TDC) was dissolved in 10 mL ethanol solution, which was then mixed with 20 mL ethanol solution containing of 50 mg  $InCl_3 \cdot 4H_2O$  and 50 mg  $Cd(Ac)_2 \cdot 3H_2O$ . The mixture was then centrifuged for 5 minutes (mins) at 10,000 rpm. The as-produced precipitate was mixed with ethanol solution containing of 100 mg TDC, and heated at 60 °C for 12 hrs. The as-obtained product was collected, and washed with copious ethanol and water, respectively.

**1.3. Synthesis of other In-MOF as control samples (30% ~100% Cd).** The synthetic procedure is similar with that of 2D In-MOF nanosheets except using different percentages of  $Cd(Ac)_2 \cdot 3H_2O$  in total metal salts ( $Cd(Ac)_2 \cdot 3H_2O$  and  $InCl_3 \cdot 4H_2O$ , 100 mg in total), for example, 40 mg  $Cd(Ac)_2 \cdot 3H_2O$  and 60 mg  $InCl_3 \cdot 4H_2O$  for In-MOF (40%Cd).

**1.4. Synthesis of 2D In-MOF nanosheets using a different intermediate agent.** In-MOF nanosheets obtained *via* a similar procedure with that of 2D In-MOF nanosheets except of replacing  $\text{Cd}(\text{Ac})_2 \cdot 3\text{H}_2\text{O}$  with  $\text{Zn}(\text{Ac})_2 \cdot 2\text{H}_2\text{O}$ .

**1.5. Synthesis of Mn-MOF nanosheets.** Mn-MOF nanosheets obtained *via* a similar procedure with that of 2D In-MOF nanosheets except of replacing  $\text{InCl}_3 \cdot 4\text{H}_2\text{O}$  with  $\text{Mn}(\text{Ac})_2 \cdot 4\text{H}_2\text{O}$ .

## **2. Physical characterization**

The morphology was observed on field emission scanning electron microscope (FESEM, JEOL 7800F), transmission electron microscope (TEM), high resolution transmission electron microscope (HRTEM, FEI Talos-F200S), and atomic force microscope (AFM, Bruker Dimension Icon). Energy-dispersive X-ray spectroscopy (EDS) and element mapping were acquired on SEM (OXFORD X-Max<sup>N</sup> 150 10 KV) and STEM (150~230Mx 200 KV). Crystal structure was examined by X-ray diffractometer (XRD, Smartlab 9 kw, 40 kV, 40 mA,  $\lambda=1.5418 \text{ \AA}$ ) with Cu-K $\alpha$  radiation. Chemical states were analyzed by X-ray photoelectron spectroscopy (XPS, Thermo ESCALAB 250XI between 0 and 1400 eV). Porosity was tested on a Micromeritics ASAP 2020 Plus analyzer by Brunauer-Emmet-Teller (BET) adsorption-desorption isotherms at 77 K. Chemical compositions of In-MOF nanosheets were determined by inductively coupled plasma mass spectrometry (ICP-MS, Thermo XSERIES 2) and thermogravimetric analysis (TGA, SDTA851E). Fourier transform infrared (FT-IR) spectra were recorded in a Thermofisher NICOLETIS 10 FTIR spectrometer. Ultraviolet visible (UV-vis) absorption spectra were recorded on Agilent Cary 60. Electrical conductivity were tested on a Signatone Four Point Probing System. <sup>1</sup>H nuclear magnetic resonance (NMR) spectra were collected on a superconducting-magnet NMR spectrometer (Bruker AVANCE III HD 500 MHz).

## **3. Electrochemical characterization**

**3.1. Preparation of working electrodes:** 5 mg as-prepared materials were dispersed in a mixed solution with 1 mL isopropanol/DI-water (v/v=4:1), containing of 1 mg acetylene black, 30  $\mu\text{L}$  Nafion

solution (5 wt%), which were ultrasonicated for 30 mins to form a uniform catalyst ink. Next, 450  $\mu\text{L}$  the above catalyst ink was transferred to a  $1.5 \times 1.5 \text{ cm}^2$  gas diffusion layer (GDL, the effective catalytic area is  $1.0 \times 1.0 \text{ cm}^2$ ) with a mass loading of  $0.2 \text{ mg cm}^{-2}$ , which was then dried under ambient conditions overnight.

**3.2. Electrochemical setup:** Nitrogen reduction reaction (NRR) was studied in a three-electrode flow-type electrochemical cell connected to CHI 760E electrochemical workstation using the above working electrode, nickel foam as the counter electrode, Ag/AgCl/KCl (saturated) as the reference electrode, Nafion 211 membrane as the separator, and 0.05 M  $\text{H}_2\text{SO}_4$  as exhaust gas absorption solution. Note that Nafion may become the ammonia contamination because it can absorb and release ammonia. Therefore, it was sequentially pretreated in  $\text{H}_2\text{O}_2$  aqueous solution (5 wt.%, 80 °C) for 3 hrs, DI-water (80 °C) for 1 hr, 0.5 M  $\text{H}_2\text{SO}_4$  solution (80 °C) for 2 hrs, 0.5 M  $\text{H}_2\text{SO}_4$  solution (100 °C) for 8 hrs, DI-water (80 °C) for 1 hr and rinsed in DI-water several times.

For NRR testing in electrolytes with different pH values, the following solutions were made: 0.05 M  $\text{H}_2\text{SO}_4$ , 0.005M  $\text{H}_2\text{SO}_4$ , 0.1 M  $\text{Na}_2\text{SO}_4$ , 0.01M KOH and 1M KOH with pH=1, 2, 7, 12 and 14, respectively. The rate of electrolyte and gas flow were kept at 40 and 20  $\text{ml min}^{-1}$ , respectively. Further, we have measured the ammonia concentration from both cathodic and anodic counterparts in the present work, which can give a more accurate evaluation of NRR performance.

**3.3. Electrochemical testing:** Before electrochemical tests, the electrolyte was purged with acid and alkaline treated Ar or  $\text{N}_2$  flows for 30 mins. To examine NRR activity, chronoamperometric testing was carried out at different currents for 1 hr. To avoid external ammonia pollution, all electrolytes were prepared fresh, and the data collected at the first cycle is discarded.

Next, the electrochemical specific surface area (ECSA) of electrodes were obtained by cyclic voltammetric curves (CVs) in a potential range of 0.5-0.6 V (vs. RHE). The data was collected at

different scan rates of 10-50 mV s<sup>-1</sup>. The plots of  $\Delta J (J_a - J_c, \text{mA})$  at 0.45 V (vs. RHE) against scan rates are nearly linear, and then the double layer capacitance  $C_{dl}$  (mF) can be obtained. In detail, the ECSA value can be calculated by the following formula:

$$\text{ECSA} = C_{dl} / C_s$$

Where  $C_s = 0.035 \text{ mF cm}^{-2}$  (the benchmark value).<sup>1</sup>

Further, electrochemical impedance spectroscopy (EIS) was tested at the open circuit potential (OCP) with the frequency ranging from 10<sup>5</sup> to 0.01 Hz.

### 3.4. Calculations for the NH<sub>3</sub> yield rate and Faradic efficiency (FE)

The yield rate of ammonia formation is calculated using the following equation:

$$Y(\text{NH}_3) = c(\text{NH}_3) \times V / (t \times m)$$

And Faradaic efficiency is calculated as follows:

$$FE = 3F \times c(\text{NH}_3) \times V / (17 \times Q)$$

where  $c(\text{NH}_3)$  is ammonia concentration,  $F$  is Faradaic constant,  $V$  is the volume of electrolyte,  $t$  is reaction time, and  $m$  is catalyst mass.

## 4. Determination of NH<sub>3</sub> by the indophenol blue method

### 4.1. Preparation of chromogenic reagents

2 mL of 1 M NaOH aqueous solution was dissolved in 5 wt% of sodium citrate and 5 wt% of salicylic acid, which was labelled as solution **A**. 1 mL of 0.05 M NaClO aqueous solution was labelled as solution **B**. While 0.2 mL of 1 wt% C<sub>5</sub>FeN<sub>6</sub>Na<sub>2</sub>O aqueous solution was labelled as solution **C**.

### 4.2. Preparation of test solutions

After chronoamperometric tests, the cathode solution, anode solution, and exhaust gas absorption liquid were collected for chromogenic tests. In addition, the Nafion separation membrane was also soaked in 5 mL of 0.5 M sulfuric acid for 24 hrs and diluted to 50 mL for chromogenic tests.

#### **4.3. UV-vis measurements**

Firstly, 2 mL of the above test solution was mixed with color reagents A, B and C in sequence. Next, the mixed solution was left in dark under ambient conditions for 2 hrs, and then subjected to UV-vis measurements in the range of 550-750 nm. The amount of ammonia was determined by comparing the UV-vis absorption peaks at 650 nm of test solutions collected from Ar and N<sub>2</sub>-saturated electrochemical cells.

#### **5. Determination of possible N<sub>2</sub>H<sub>4</sub> byproduct using Watt-Chrisp method**

A mixture solution of para-(dimethylamino) benzaldehyde (5.99 g), HCl (concentrated, 30 mL) and ethanol (300 mL) was prepared as the coloring reagent. Then, an equal amount of coloring reagent was mixed with the test solution, which was left in dark under ambient conditions for 30 mins before UV-vis measurements at 455 nm.

#### **6. <sup>15</sup>N<sub>2</sub> isotope experiments**

Isotopic labelling experiments with acid and alkaline treated <sup>15</sup>N<sub>2</sub> feeding gas can identify possible external pollution, and thus been used to verify source of ammonia during NRR. Before the isotopic experiment, Ar gas was continuously passed through the NRR electrolytic cell for 30 mins. Next, NRR testing was carried out for 20 hrs in a closed circulation electrochemical system saturated with <sup>15</sup>N gas with a flow rate of 20 mL min<sup>-1</sup>. Finally, the electrolyte was collected, adjusted to pH=2, and then concentrated for <sup>1</sup>H NMR analysis.

#### **7. DFT calculation details**

Computation were conducted according to density functional theory (DFT). The ionic cores were illustrated by the projector-augmented wave (PAW) method. The Perdew-Burke-Ernzerhof (PBE)<sup>2</sup> functional with and without the correction of van der Waals forces (by Grimme method) was used for electron exchange-correlation within generalized gradient approximation (GGA) implemented in VASP package code.<sup>3,4</sup> Cut-off energy for plane wave expansion was fixed at 400 eV, optimized from a range of cut-off energies. Electronic self-consistent-loop criterion was set to  $10^{-4}$  eV. During geometry optimization, the structures were relaxed to forces on all atoms smaller than 0.05 eV/Å. A Gaussian smearing method was employed with 0.1 eV width. The K-points for structural optimization in all models were set to  $5 \times 1 \times 3$ . For density of state (DOS) calculations, the k-points were set to be  $10 \times 1 \times 6$ .

A surface was cleaved across a (030) direction to form an In-MOF slab. The slab is a sandwich structure with the top and bottom layers containing Indium atoms with the two layers linked by thiophene acid groups.

The detailed Gibbs free energy calculation for NRR has been carried out by putting a portion atom of In-MOF in a large box ( $10 \text{ \AA} \times 35 \text{ \AA} \times 14 \text{ \AA}$ ) according to the following equation:

$$G = E + \int C_P dT - TS$$

where  $G$ ,  $E$  and  $CP$  refer to the chemical potential (partial molar Gibbs free energy), electronic energy and heat capacity, respectively. The entropy term can be expressed as the sum of the translational, rotational, vibrational and electronic contributions as to:

$$S = S_t + S_r + S_v + S_e$$

And finally, intrinsic zero-point energy (ZPE) and extrinsic dispersion (D) corrections can be included to finally obtain:

$$G = E + \int C_P dT - T(S_t + S_r + S_v + S_e) + \text{ZPE} + \text{D}$$

Since  $S_e \approx 0$  at the fundamental electronic level.

For the case of solids and adsorbates, some approximations can be assumed:

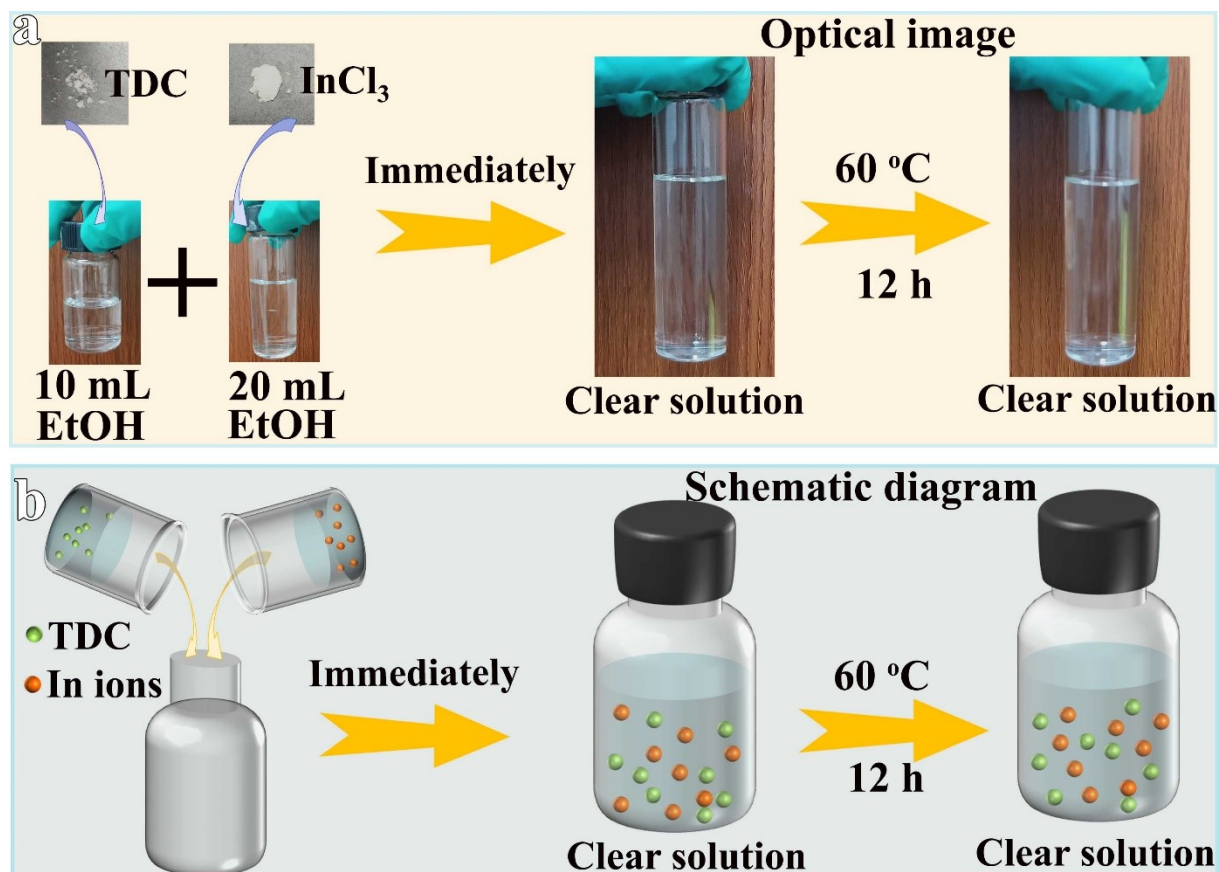
1. As for gases, at the fundamental electronic level  $S_e \approx 0$ .
2. Translational and rotational motions can be neglected, therefore,  $S_t \approx 0$  and  $S_r \approx 0$ . In this sense, all entropy contributions come from vibrations:  $S = S_v$ . Similarly, translational and rotational contributions to the heat capacity are neglected.

Therefore, Gibbs free energies for the different states have been calculated as to:

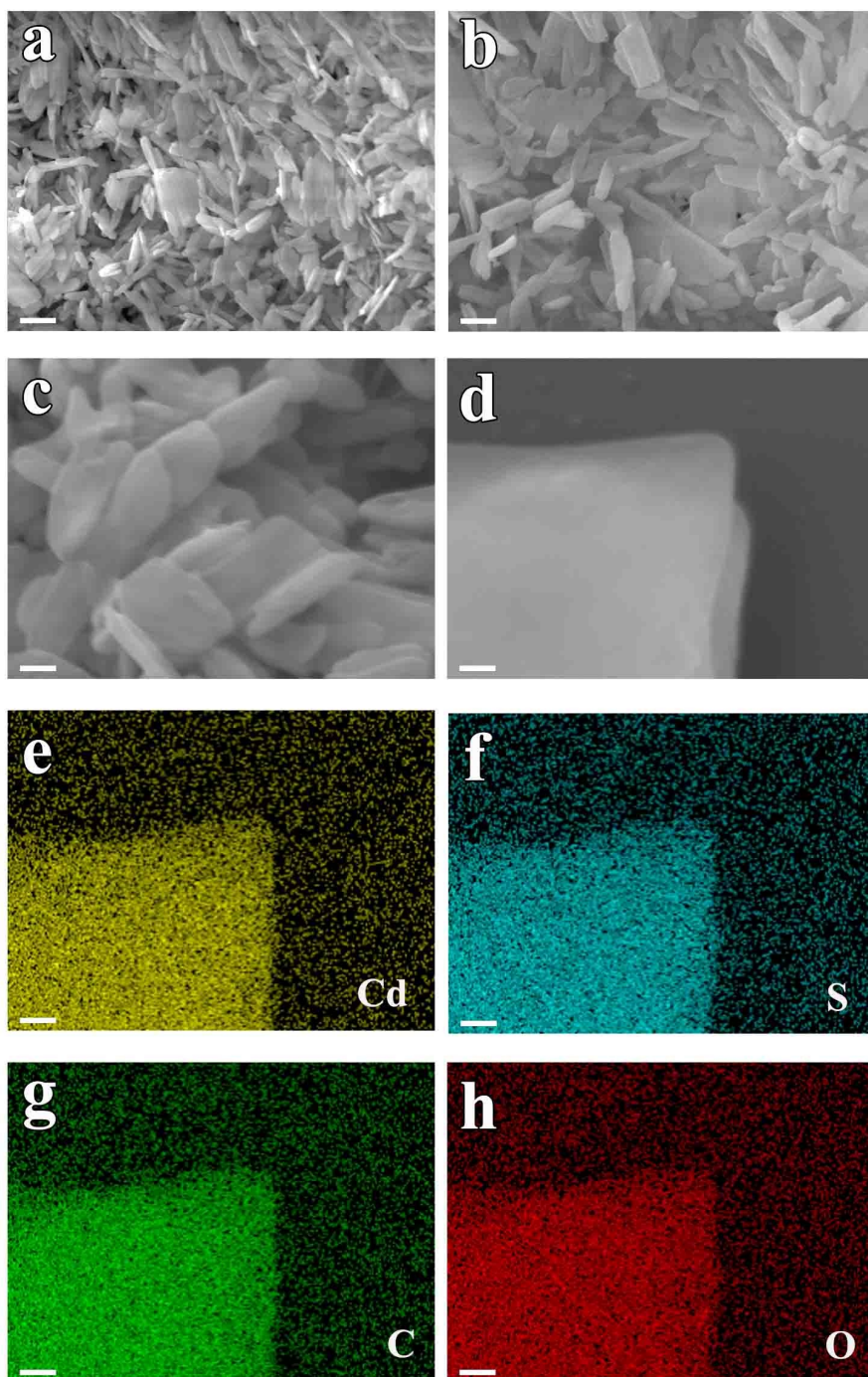
$$G = E + \int C_p dT - TS_v + \text{ZPE} + D$$

Notably, we have simulated NRR pathways with either  $\text{H}^+$  or  $\text{H}_2\text{O}$  as the proton source dependent on the pH value. In acidic electrolyte ( $\text{pH} < 7$ ), protons can directly source from  $\text{H}^+$  in electrolytes. While in neutral and alkaline electrolytes ( $\text{pH} \geq 7$ ), protons can only be available from water because of the low concentrations of  $\text{H}^+$  in electrolytes. Therefore, we have simulated the NRR reaction pathway through  $\text{N}_2$  binding with  $\text{H}^+$  ( $\text{pH} < 7$ ) or water ( $\text{pH} \geq 7$ ), which leads to ammonia ( $\text{NH}_3$ ). The overall simulation process is described in Figure 4.

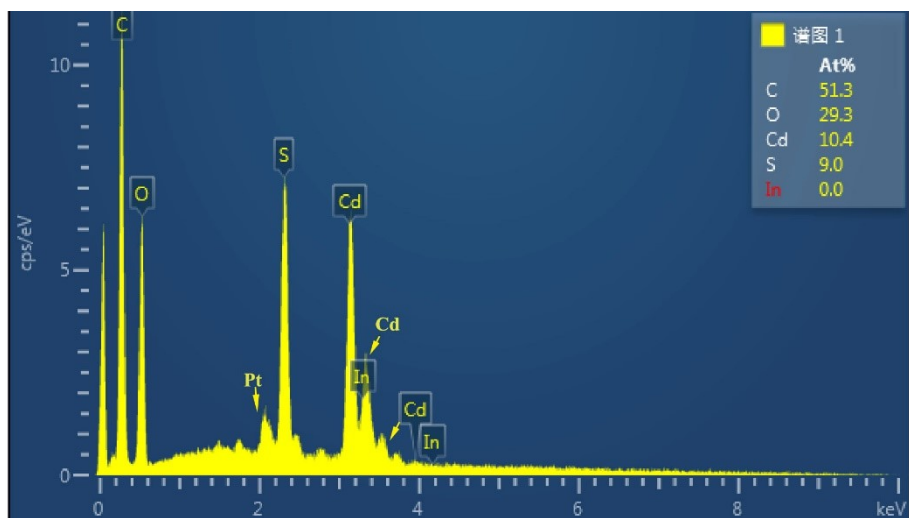
## II. Supplementary Results



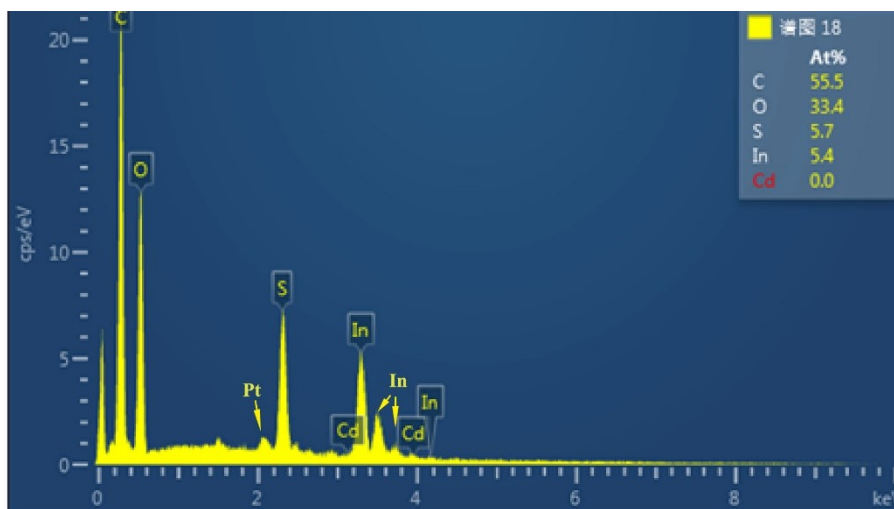
**Supplementary Fig. 1** Optical images and schematic diagram of a synthesis procedure similar with that of 2D In-MOF nanosheets, except only using  $\text{InCl}_3 \cdot 4\text{H}_2\text{O}$  and TDC as precursors without  $\text{Cd}(\text{Ac})_2 \cdot 3\text{H}_2\text{O}$ . After the mixed solution being kept for 12 hrs at 60 °C, it remains a clear solution. This phenomenon indicates that  $\text{InCl}_3 \cdot 4\text{H}_2\text{O}$  cannot interact with TDC to form a MOF structure directly. Therefore,  $\text{Cd}(\text{Ac})_2 \cdot 3\text{H}_2\text{O}$  plays an important role during the formation of In-MOF nanosheets.



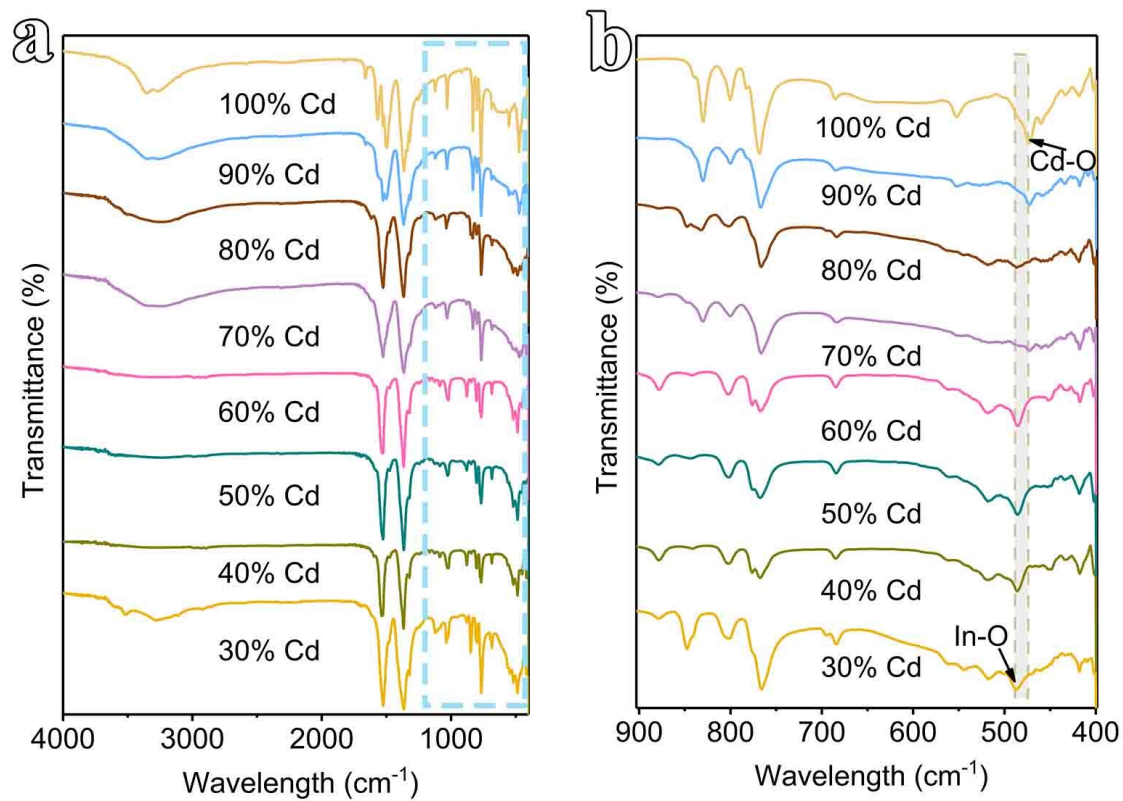
**Supplementary Fig. 2** Morphological characterization of Cd-MOF control sample synthesized by using 100% Cd precursor. (a-d) SEM images (scale bars for a, b, c and d are 1 μm, 500 nm, 500 nm and 200 nm). (e-h) SEM elemental mappings of Cd, S, C, O (scale bars: 200 nm).



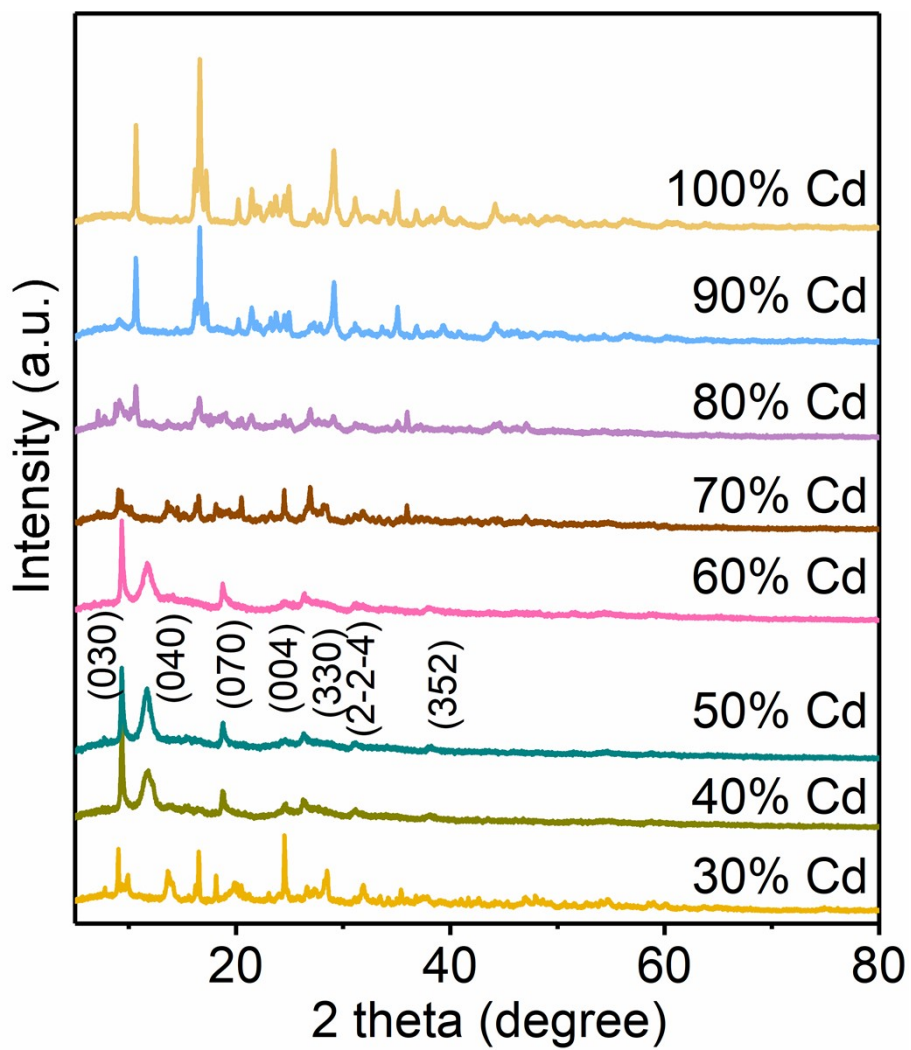
**Supplementary Fig. 3** EDS profile of Cd-MOF control sample synthesized by using 100% Cd precursor.



**Supplementary Fig. 4** EDS profile of In-MOF nanoparticle precursor obtained by directly mixing 50 mg of  $\text{InCl}_3 \cdot 4\text{H}_2\text{O}$  and 50 mg of  $\text{Cd}(\text{Ac})_2 \cdot 3\text{H}_2\text{O}$  with 100 mg of organic ligand (TDC). It is shown that no Cd has been detected in the as-formed product.



**Supplementary Fig. 5** FT-IR spectra of In-MOF control samples synthesized by using different amounts of Cd precursors. Panel **b** is an enlarged area of panel **a**.

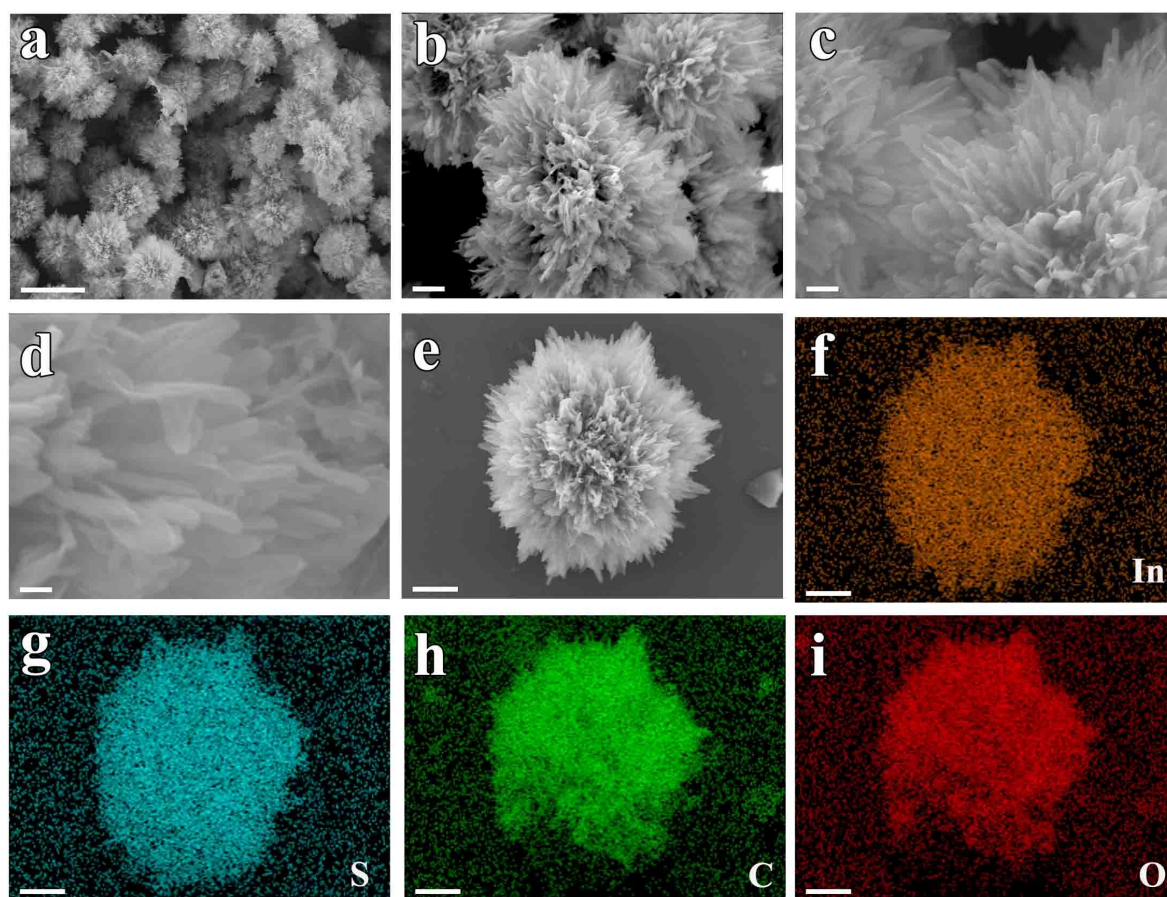


**Supplementary Fig. 6** XRD patterns of as-prepared In-MOF samples by using different amounts of Cd precursors.

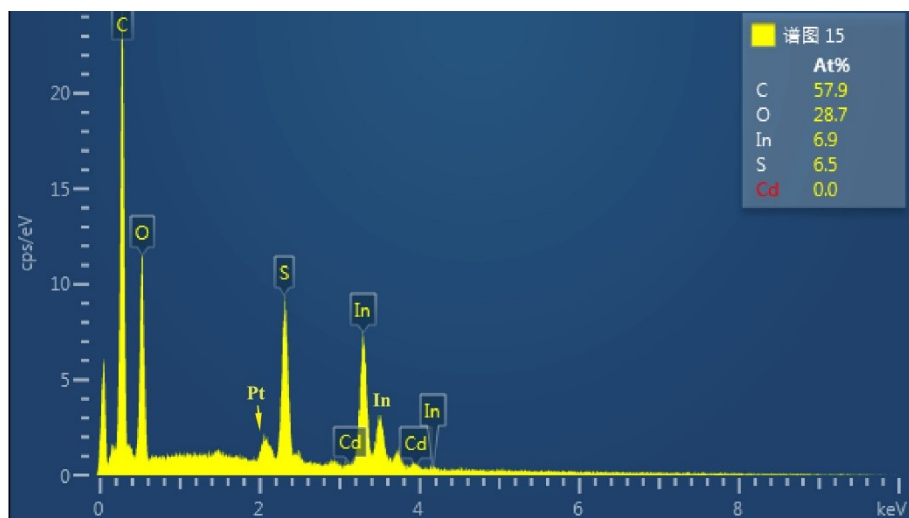
## Supporting Note 1:

To explore influence of  $\text{Cd}^{2+}$  on the synthesis of In-MOF, we have examined the different mass percentages of the Cd salt ( $\text{Cd}(\text{Ac})_2 \cdot 3\text{H}_2\text{O}$ ) in total metal salts ( $\text{Cd}(\text{Ac})_2 \cdot 3\text{H}_2\text{O} + \text{InCl}_3 \cdot 4\text{H}_2\text{O}$ ). The results are shown in Supplementary Figs. 2, 3 and 5-12. When the mass percentage of Cd salt is in the range of 0%-20%, no obvious products form, so we do not present any data here. While with the weight percent of Cd salt in the range of 30%-100%, white products of In-MOF, InCd-MOF or Cd-MOF have been observed. The FT-IR in Supplementary Fig. 5 shows an obvious In-O bond at  $488 \text{ cm}^{-1}$  with 30%-80% Cd, and Cd-O bond at  $473 \text{ cm}^{-1}$  with 90%-100% Cd. This result is consistent with other characterization including XRD (Supplementary Fig. 6), SEM, EDS element mappings and spectra (Supplementary Figs. 2, 7-12), all of which shows that pure In-MOF phase has formed with 30%-80% Cd salt, while InCd-MOF for 90% Cd salt, and Cd-MOF for 100% Cd salt.

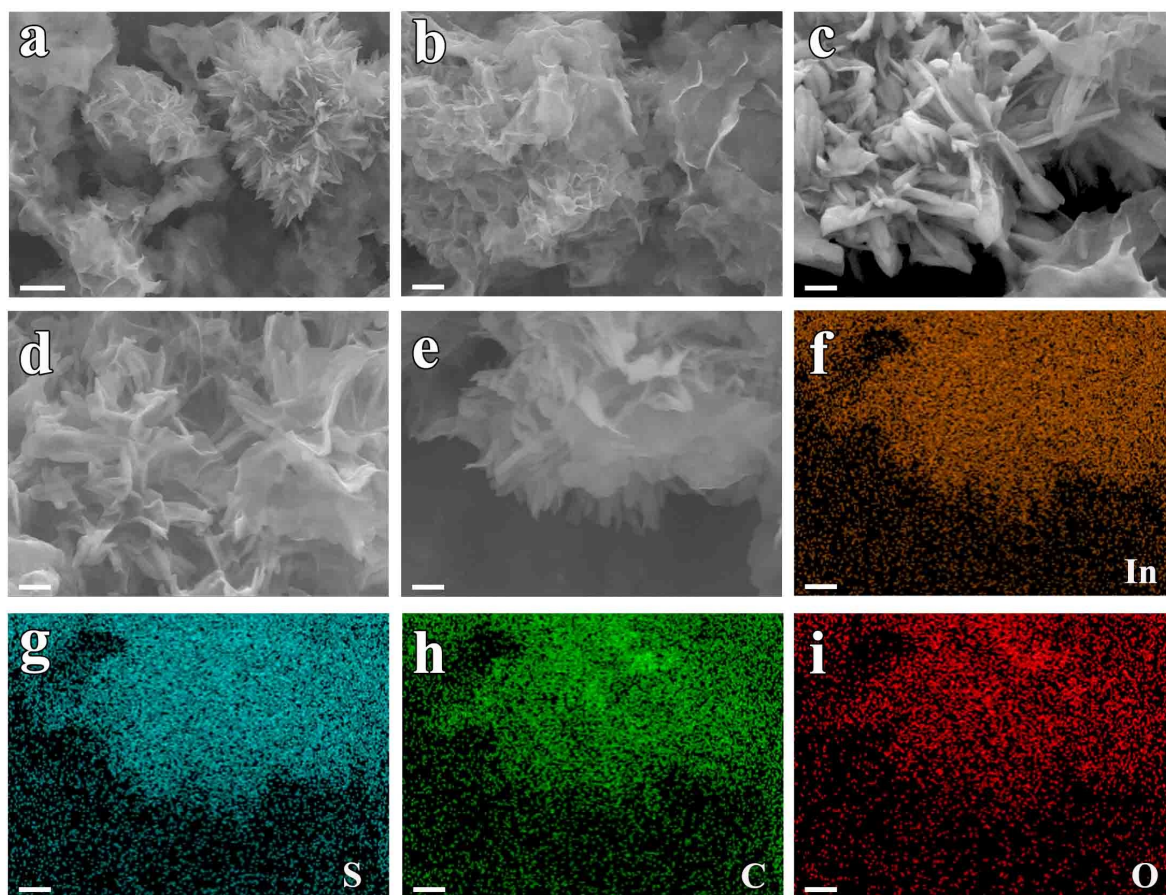
In addition, SEM images indicate morphology of the MOF material change significantly, for example, nanoflowers for 30% Cd salt (Supplementary Fig. 7), mixture of nanosheets and nanoneedles for 40% Cd salt (Supplementary Fig. 9), well-defined nanosheets for 50%~80% Cd salt (Fig. 2), mixture of nanosheets and nanorods for 90% Cd salt (InCd-MOF, Supplementary Fig. 11) and microscopic particles for 100% Cd salt (Cd-MOF, Supplementary Fig. 2).



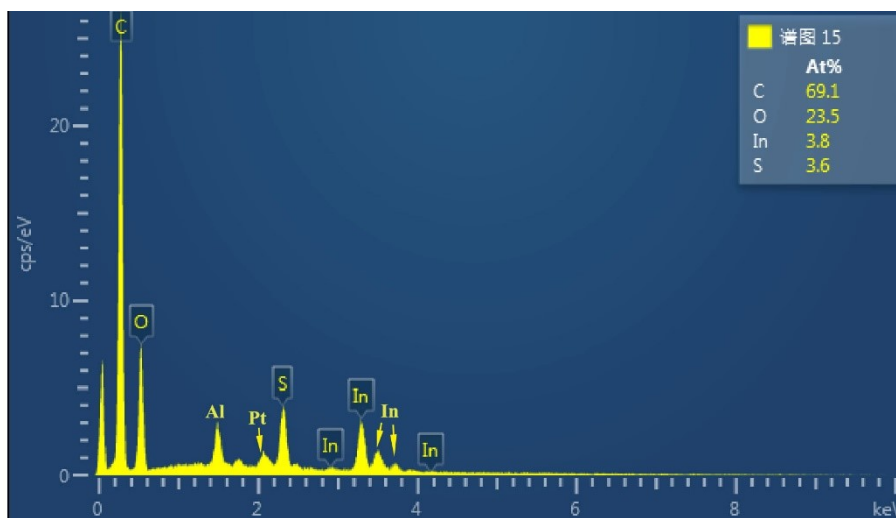
**Supplementary Fig. 7** Morphological characterization of In-MOF control sample synthesized by using 30% Cd salt. (a-e) SEM images (scale bars for a, b, c, d and e are 10  $\mu\text{m}$ , 1  $\mu\text{m}$ , 500 nm, 200 nm, and 2  $\mu\text{m}$ ). (f-i) SEM elemental mappings of In, S, C, O (scale bar: 2  $\mu\text{m}$ ).



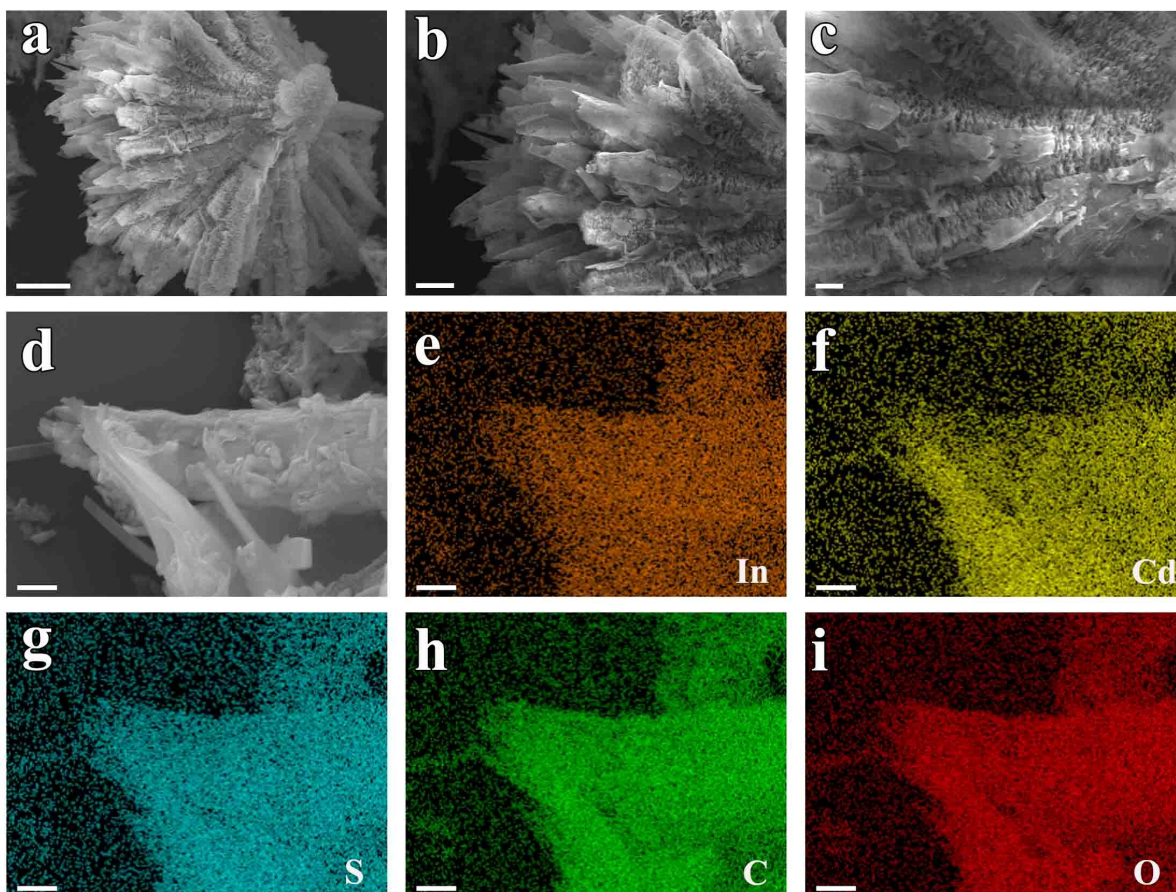
**Supplementary Fig. 8** EDS profile of In-MOF control sample synthesized by using 30% Cd salt.



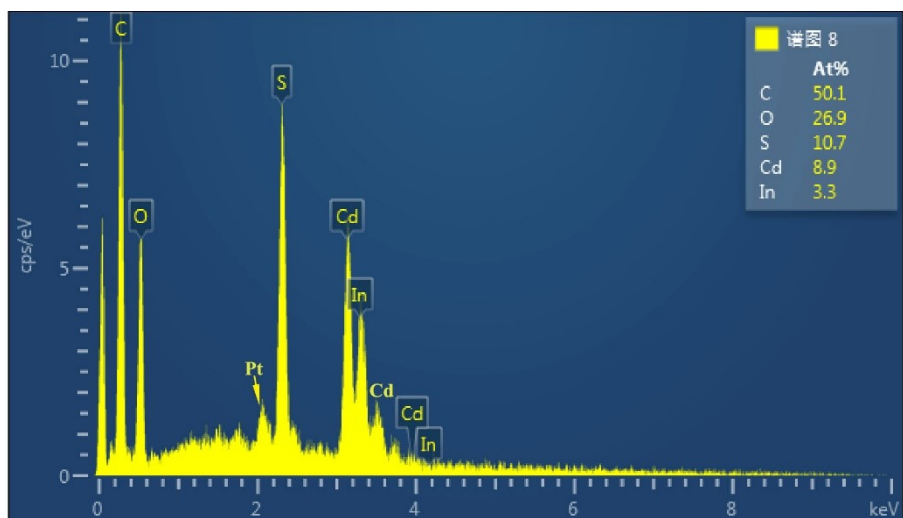
**Supplementary Fig. 9** Morphological characterization of In-MOF control sample synthesized by using 40% Cd salt. (a-e) SEM images (scale bars for a, b, are 2  $\mu\text{m}$ , 1  $\mu\text{m}$ , c-e are 500 nm). (f-i) SEM elemental mappings of In, S, C, O (scale bar: 500 nm).



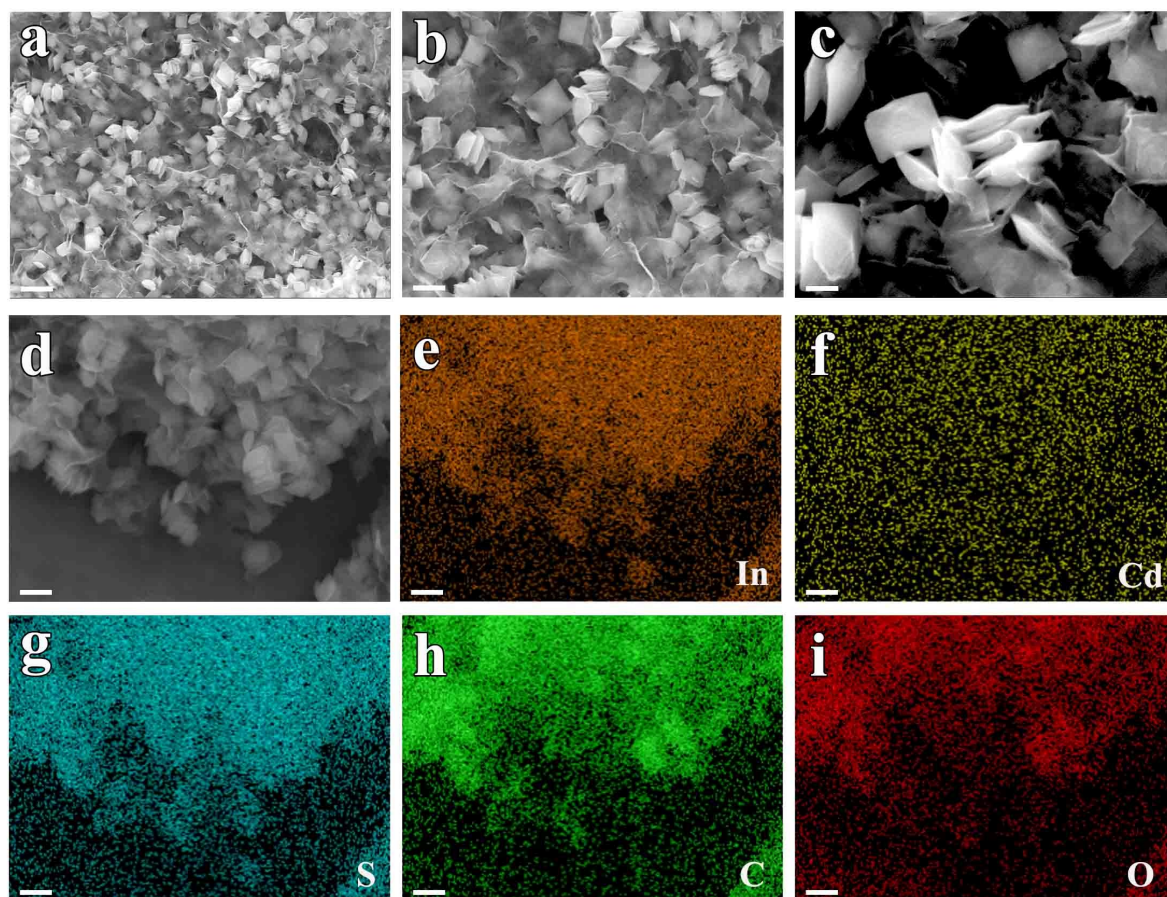
**Supplementary Fig. 10** EDS profile of In-MOF control sample synthesized by using 40% Cd salt.



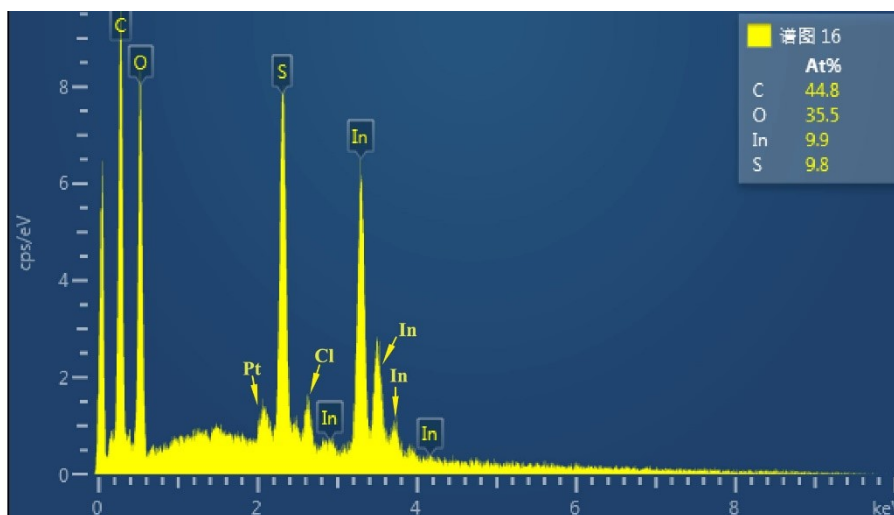
**Supplementary Fig. 11** Morphological characterization of InCd-MOF control sample synthesized by using 90% Cd salt. (a-d) SEM images (scale bars for a, b, c and d are 5  $\mu\text{m}$ , 2  $\mu\text{m}$ , 1  $\mu\text{m}$  and 500 nm). (e-i) SEM elemental mappings of In, Cd, S, C, O (scale bar: 500 nm).



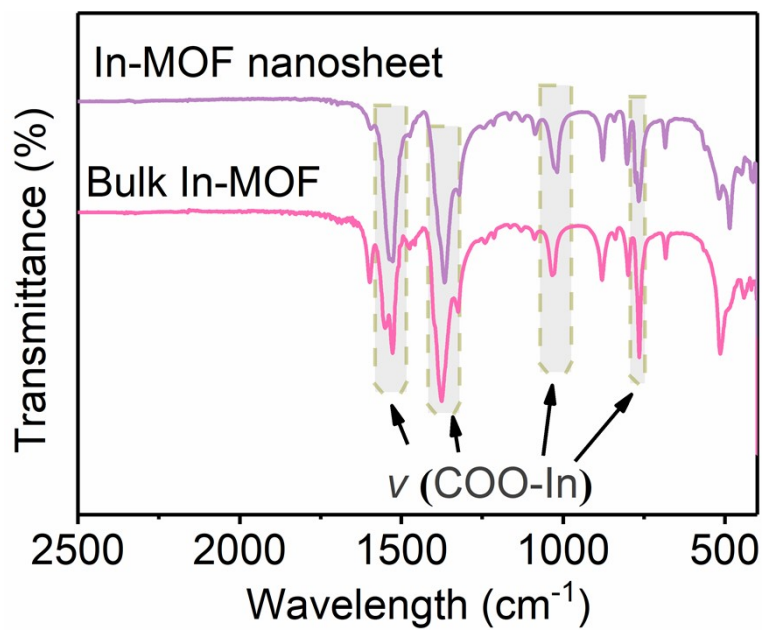
**Supplementary Fig. 12** EDS profile of InCd-MOF control sample synthesized by using 90% Cd salt.



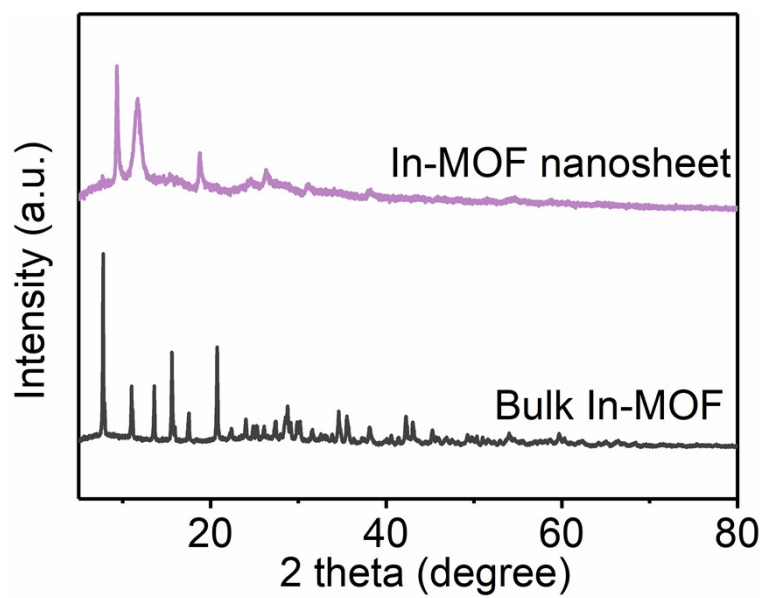
**Supplementary Fig. 13** Morphological characterization of bulk In-MOF with the particle size of several micrometers. (a-d) SEM images (scale bars for a, b, c and d are 1  $\mu\text{m}$ , 500, 200, and 500 nm). (e-i) SEM elemental mappings of In, Cd, S, C, O (scale bar: 500 nm).



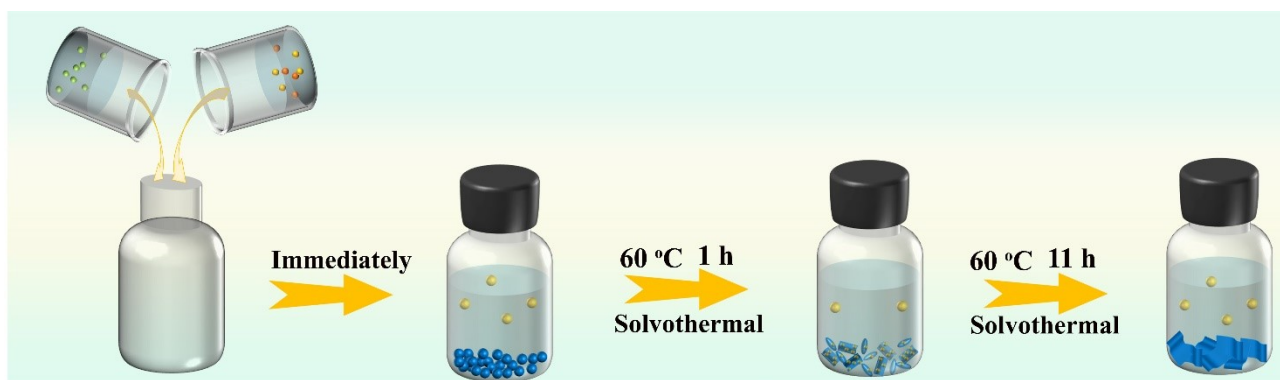
**Supplementary Fig. 14** EDS profile of bulk In-MOF.



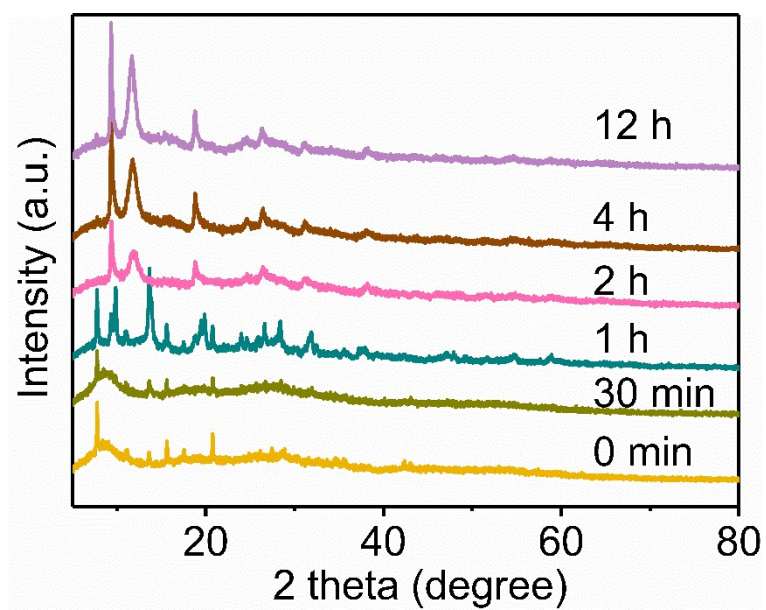
**Supplementary Fig. 15** FT-IR spectra of 2D In-MOF nanosheets and bulk MOF.



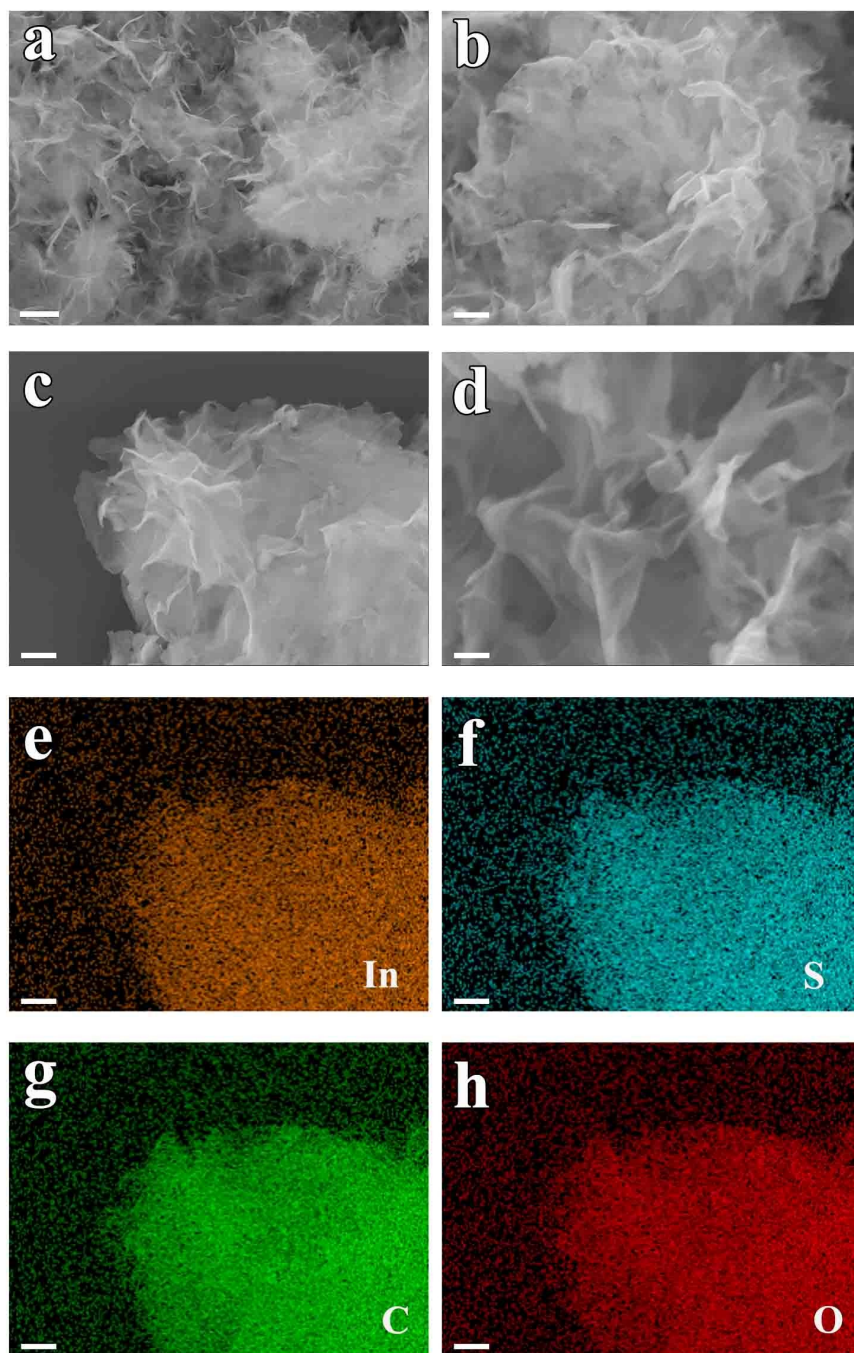
**Supplementary Fig. 16** XRD patterns of 2D In-MOF nanosheet and bulk MOF.



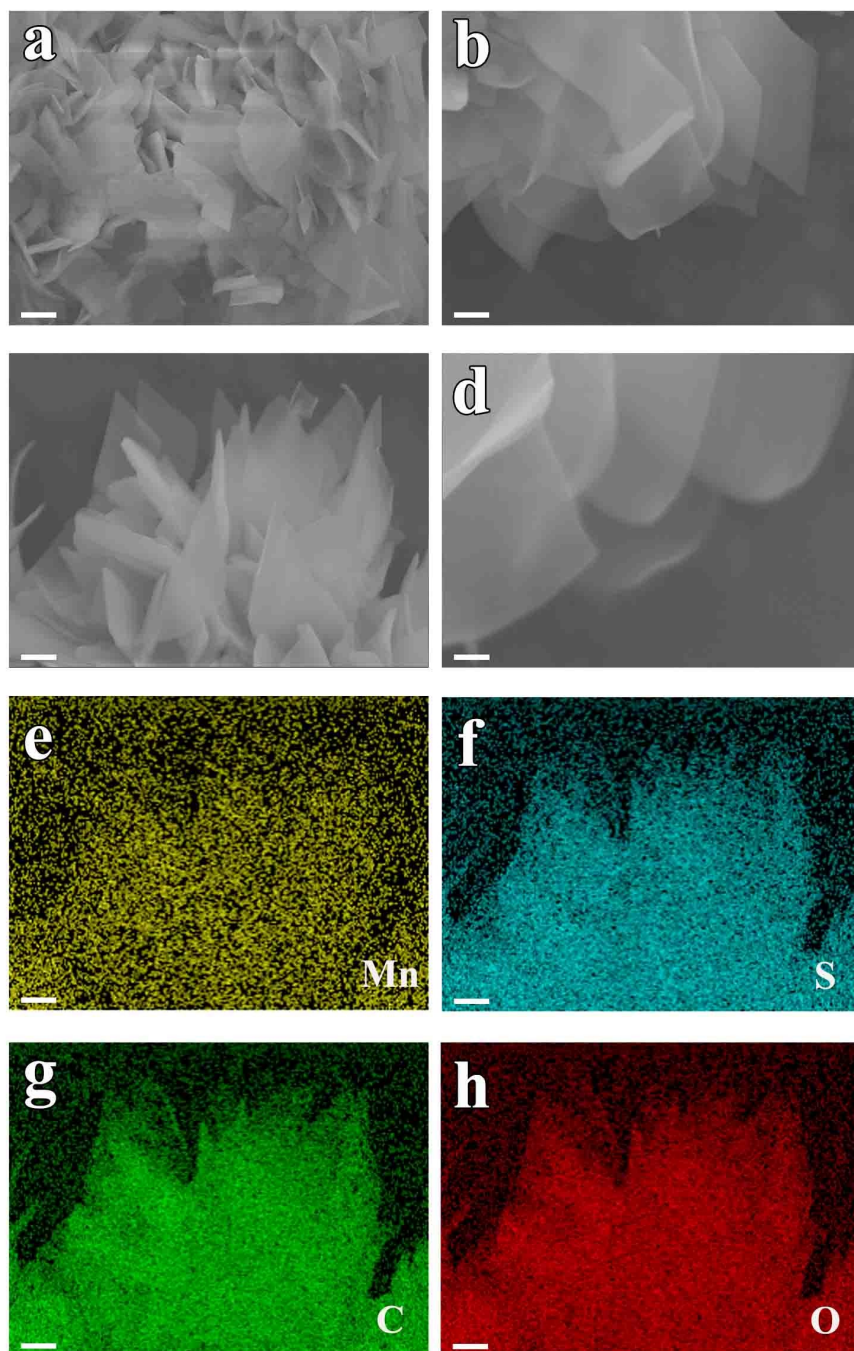
**Supplementary Fig. 17** Schematic synthesis of 2D In-MOF nanosheets through a controlled reaction process. Among all reaction precursors (Fig. 1b), only the organic ligand of TDC exhibits an UV-vis absorption peak at a wavelength range of 350-400 nm. Therefore, the reaction process can be monitored through the TDC signal using UV-vis spectra. As shown in Fig. 1c, the intensity of UV-vis spectra does not change after 4 hrs, indicating the reaction process has completed by then. This result is consistent with that from FT-IR spectra in Fig. 1d. Further, SEM images show that more In-MOF nanosheets appear with the depletion of large particles (Fig. 1e), which indicates the dissolution-recrystallization mechanism is responsible for the reaction process.



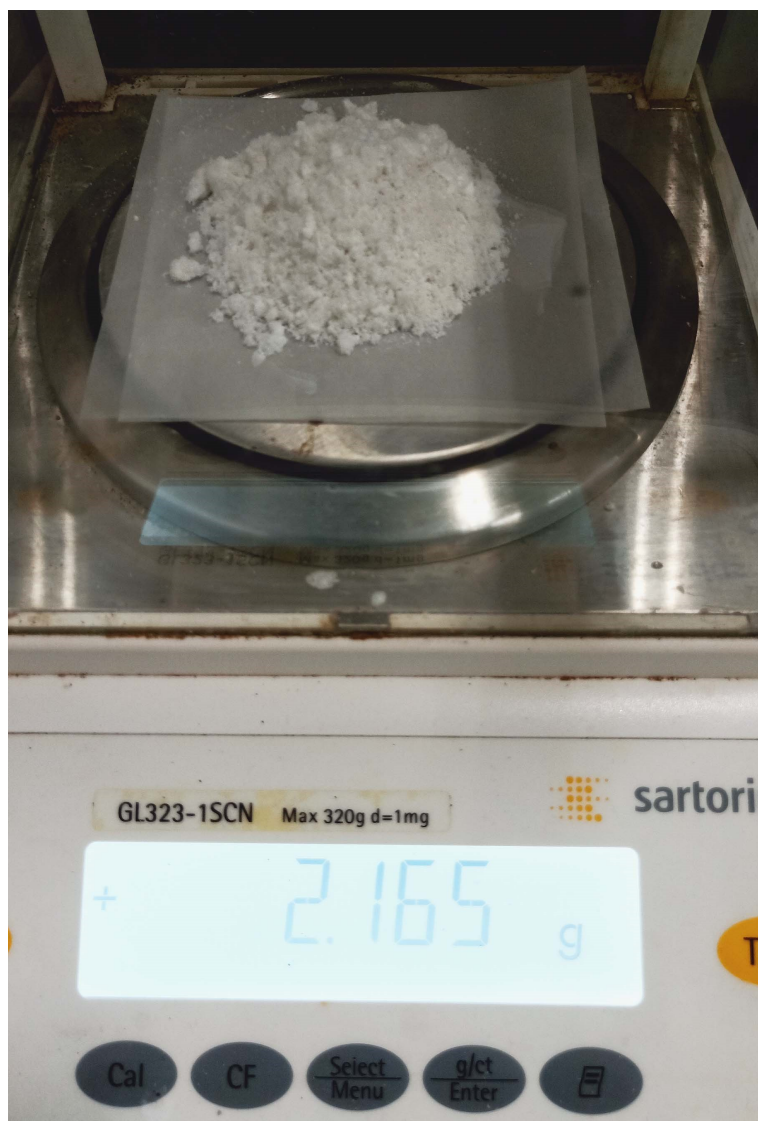
**Supplementary Fig. 18** XRD patterns of intermediates collected at different reaction durations during synthesis of 2D In-MOF nanosheets.



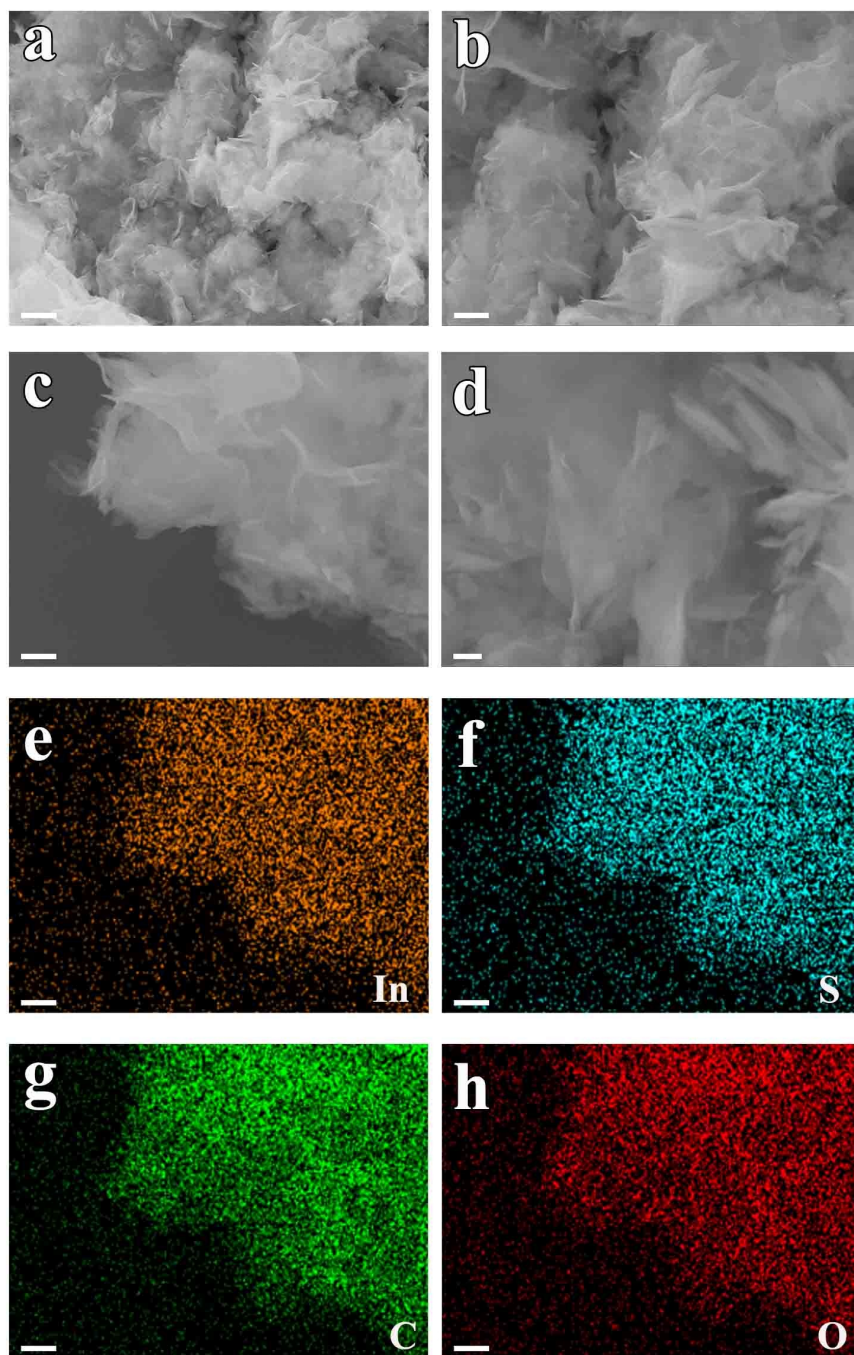
**Supplementary Fig. 19** Morphological characterization of 2D In-MOF control sample prepared using a different intermediate by replacing  $\text{Cd}(\text{Ac})_2 \cdot 3\text{H}_2\text{O}$  with  $\text{Zn}(\text{Ac})_2 \cdot 2\text{H}_2\text{O}$ . (a-d) SEM images (scale bars for a, b, c and d are 2  $\mu\text{m}$ , 500 nm, 500 nm and 200 nm). (e-h) SEM elemental mappings of In, S, C, O (scale bar: 500 nm).



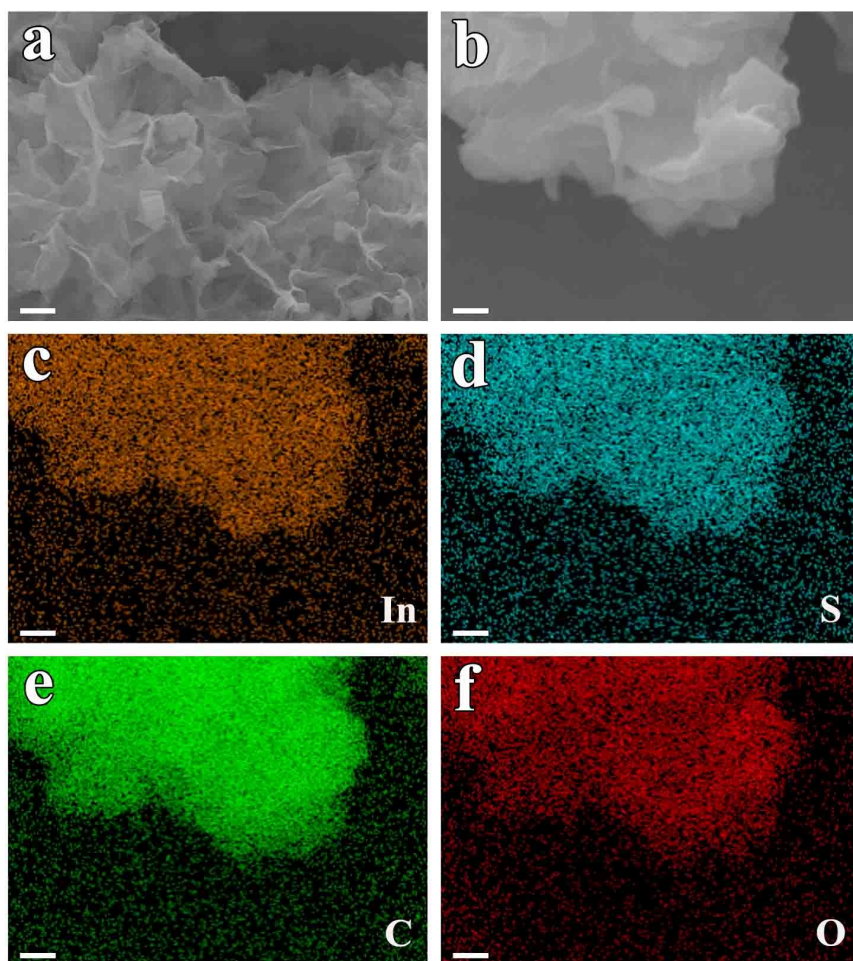
**Supplementary Fig. 20** Morphological characterization of Mn-MOF control sample synthesized *via* a similar procedure except of replacing the  $\text{InCl}_3 \cdot 4\text{H}_2\text{O}$  precursor with  $\text{Mn}(\text{Ac})_2 \cdot 4\text{H}_2\text{O}$ . (a-d) SEM images (scale bars for a, b, c and d are 1  $\mu\text{m}$ , 500 nm, 500 nm and 200 nm). (e-h) SEM elemental mappings of Mn, S, C, O (scale bar: 500 nm).



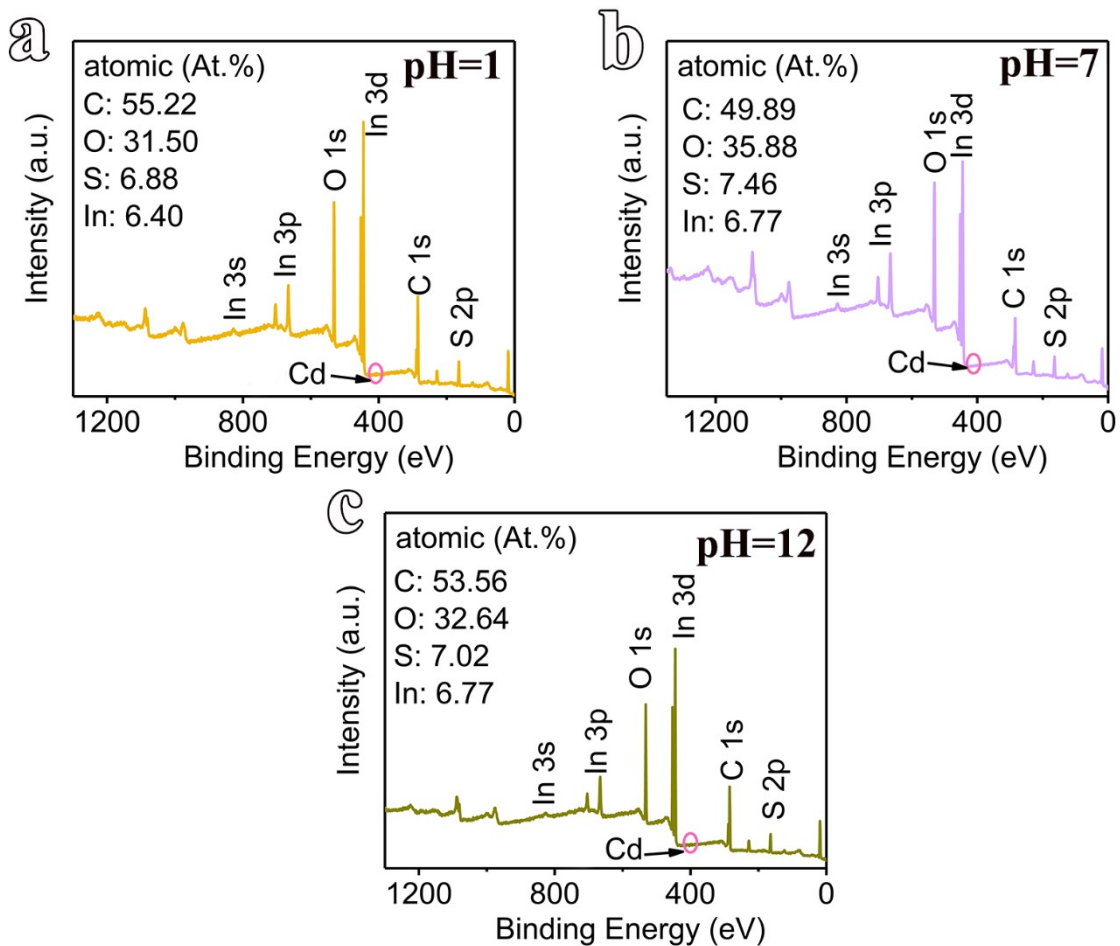
**Supplementary Fig. 21** An optical image of 2D In-MOF nanosheets obtained from a large-scale synthesis procedure in a 1-liter container, which indicates a product yield of 2.165 grams.



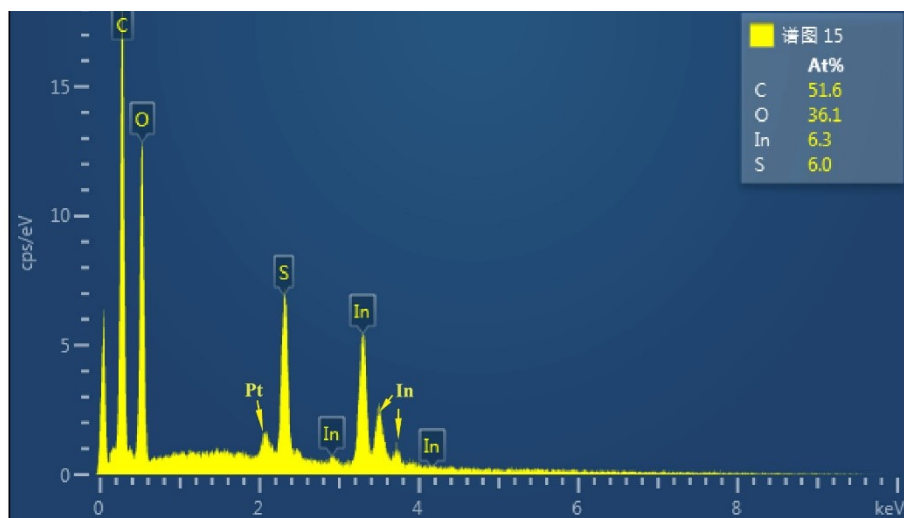
**Supplementary Fig. 22** Morphological characterization of 2D In-MOF nanosheet after being treated in 0.05 M  $\text{H}_2\text{SO}_4$  (pH=1) for 24 hrs. (a-d) SEM images (scale bars for a, b, c and d is 2  $\mu\text{m}$ , 1  $\mu\text{m}$ , 500 nm and 200 nm). (c-f) SEM elemental mappings of In, S, C, O (scale bar: 500 nm).



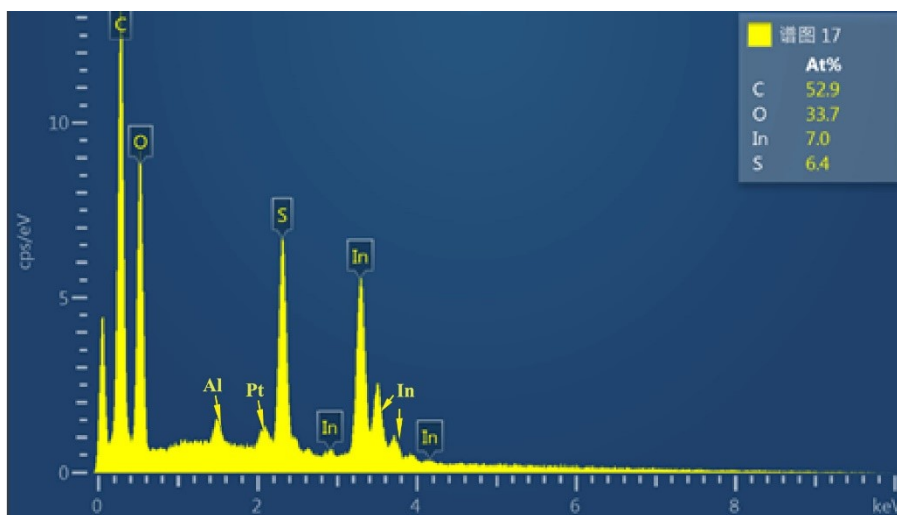
**Supplementary Fig. 23** Morphological characterization of 2D In-MOF nanosheet after being treated in 0.01 M KOH (pH=12) for 24 hrs. (a, b) SEM images (scale bars for a and b are 500 nm and 200 nm). (c-f) SEM elemental mappings of In, S, C, O (scale bar: 200 nm).



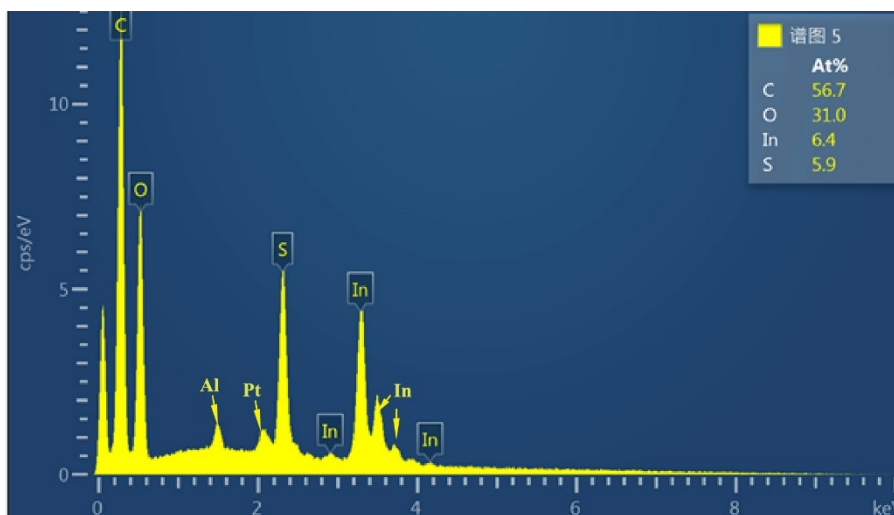
**Supplementary Fig. 24** XPS survey scans of 2D In-MOF nanosheets after treatment in solutions with different pH values.



**Supplementary Fig. 25** EDS profile of 2D In-MOF nanosheets without any treatment.



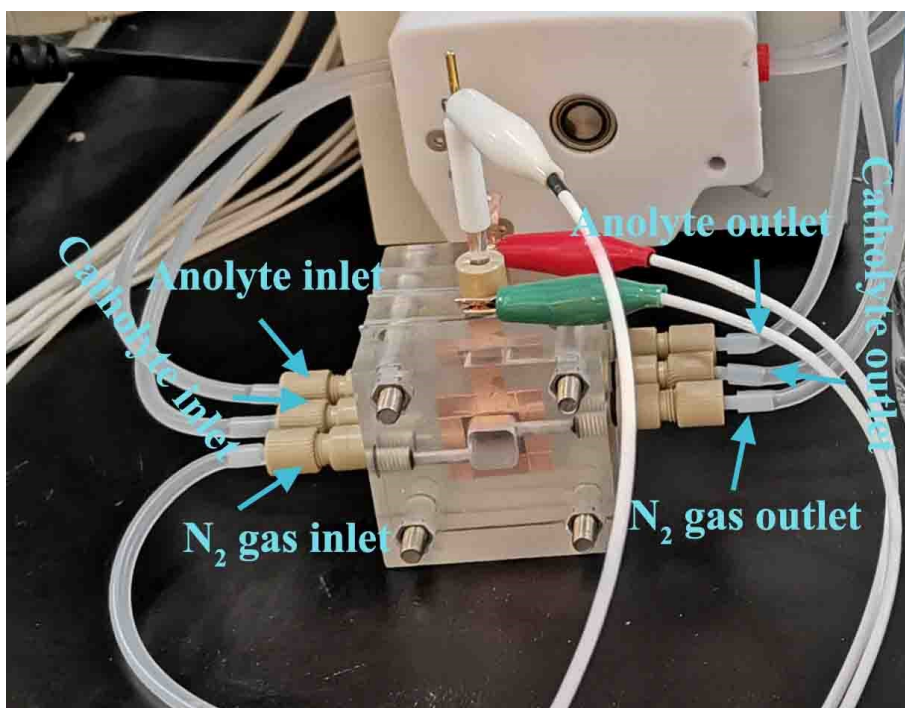
**Supplementary Fig. 26** EDS profile of 2D In-MOF nanosheets after being treated in 0.05 M H<sub>2</sub>SO<sub>4</sub> (pH=1) for 24 hrs.



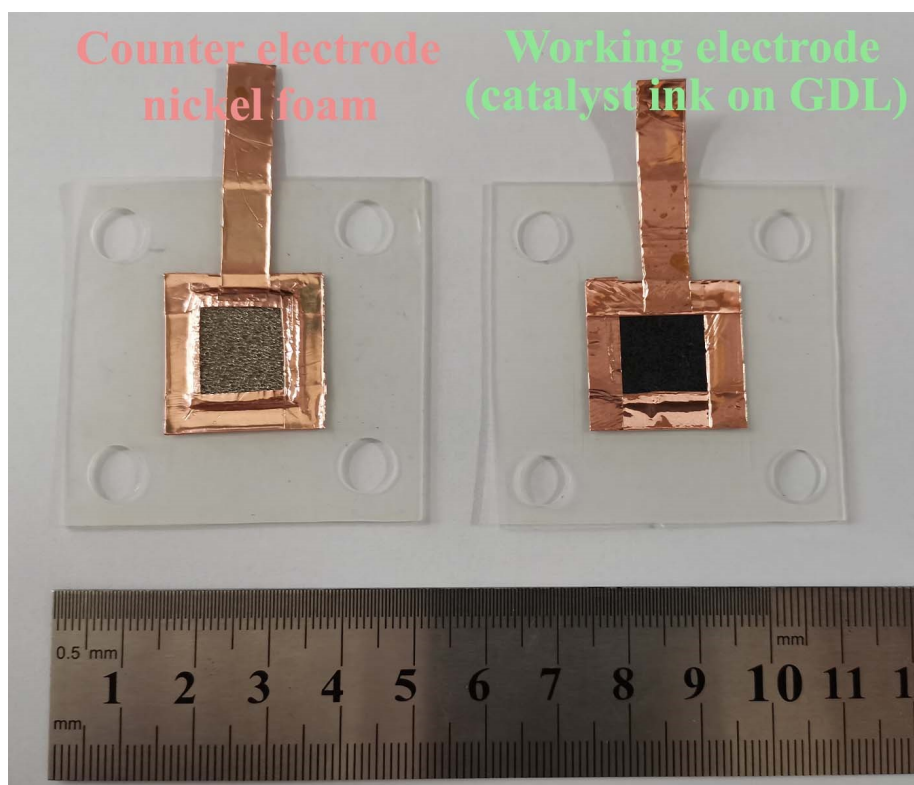
**Supplementary Fig. 27** EDS profile of 2D In-MOF nanosheets after being treated in 0.01 M KOH (pH=12) for 24 hrs.



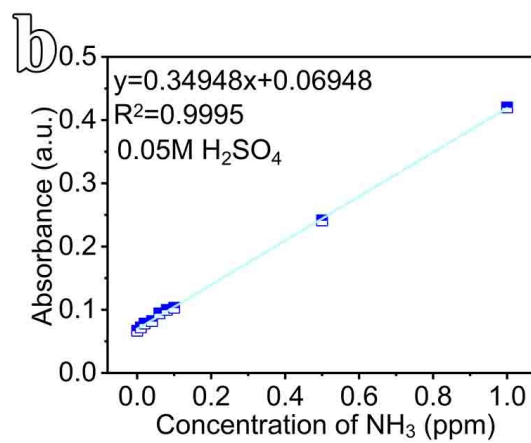
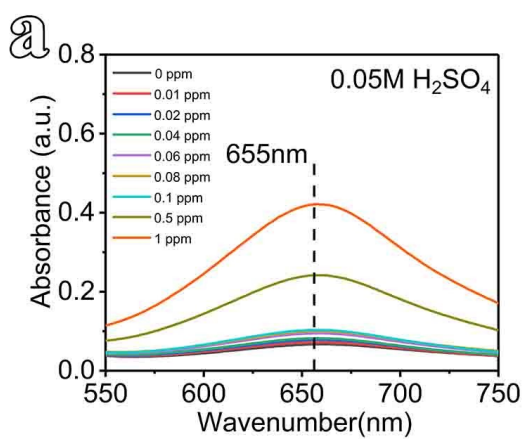
**Supplementary Fig. 28** The electrochemical cell configuration for NRR, which includes a catholyte chamber, anolyte chamber, acid absorbent chamber 1, acid absorbent chamber 2, and liquid seal chamber for the electrolyte and  $\text{NH}_3$  product.



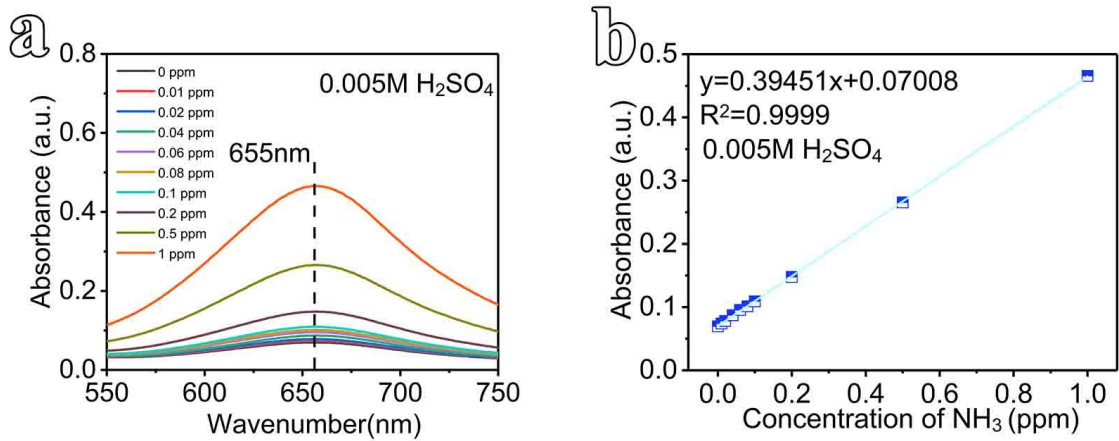
**Supplementary Fig. 29** An enlarged optical image of an electrochemical cell configuration for NRR.



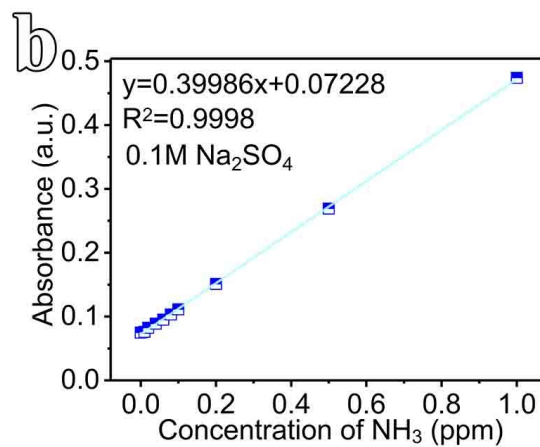
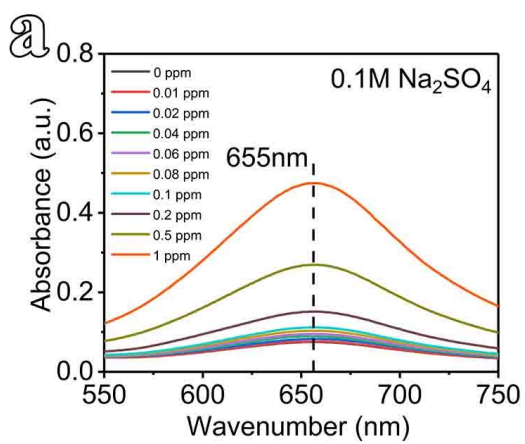
**Supplementary Fig. 30** An optical image of a counter and working electrode on conductive tape substrates. As shown in Supplementary Fig. 30, a piece of copper tape holds the anode and cathode in place while acting as a conducting connection between the electrode and the external path. The cutting area for working and counter electrodes is  $1.5 \times 1.5 \text{ cm}^2$ , and the effective active area is  $1 \times 1 \text{ cm}^2$ . The excess edges are in contact with copper tape fixed *via* PTFE separators by the reactor frame. Therefore, only the catalyst is exposed to electrolytes during experiments.



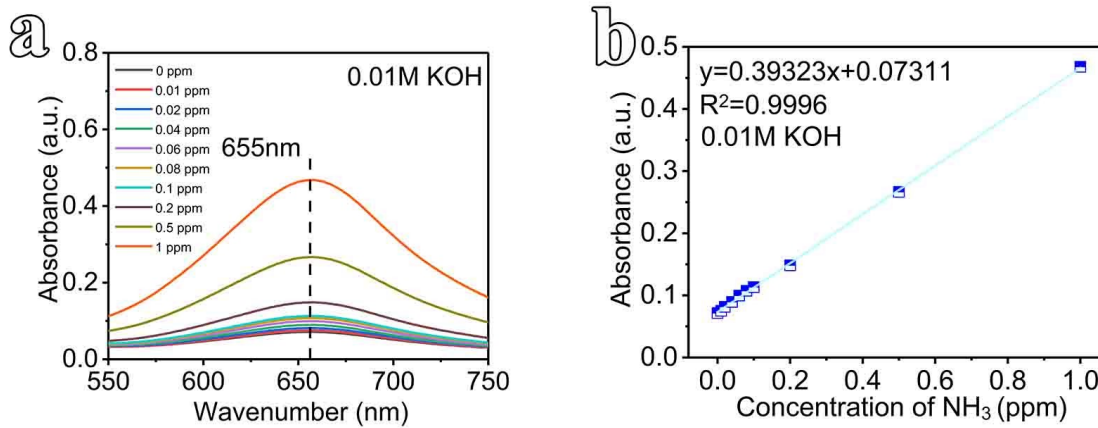
**Supplementary Fig. 31** Calibration curves for NH<sub>4</sub>Cl in **0.05 M H<sub>2</sub>SO<sub>4</sub>** solution. (a) UV-vis absorption spectra; (b) the calibration curve.



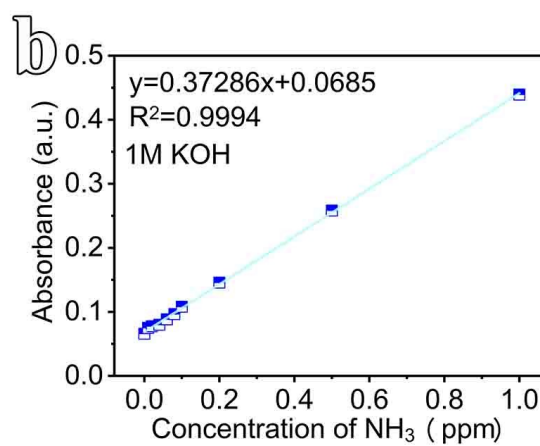
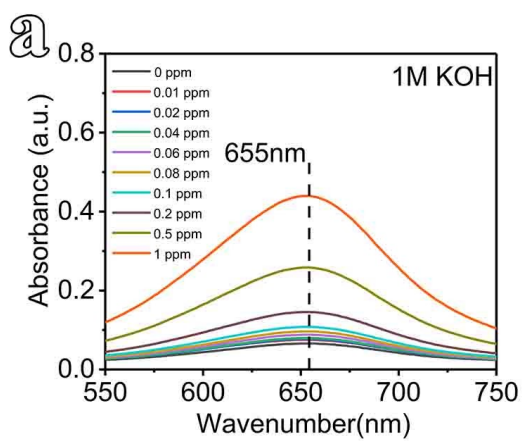
**Supplementary Fig. 32** Calibration curves for  $\text{NH}_4\text{Cl}$  in  $0.005\text{ M H}_2\text{SO}_4$  solution. (a) UV-vis absorption spectra; (b) the calibration curve.



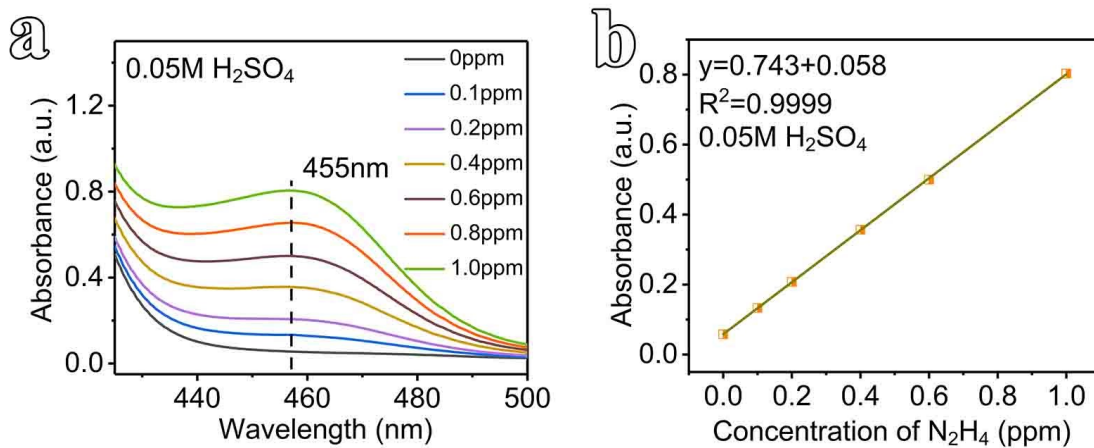
**Supplementary Fig. 33** Calibration curves for  $\text{NH}_4\text{Cl}$  in  $0.1 \text{ M Na}_2\text{SO}_4$  solution. (a) UV-vis absorption spectra; (b) the calibration curve.



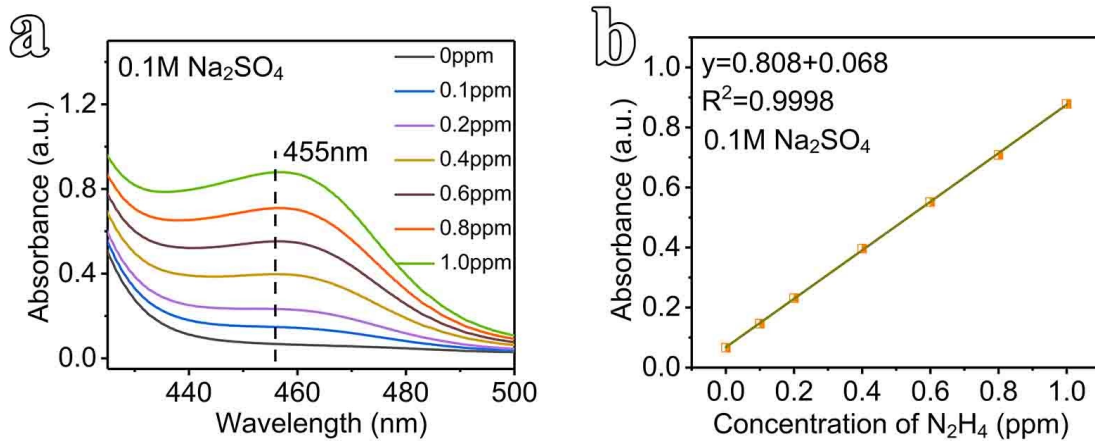
**Supplementary Fig. 34** Calibration curves for  $\text{NH}_4\text{Cl}$  in **0.01 M KOH** solution. (a) UV-vis absorption spectra; (b) the calibration curve.



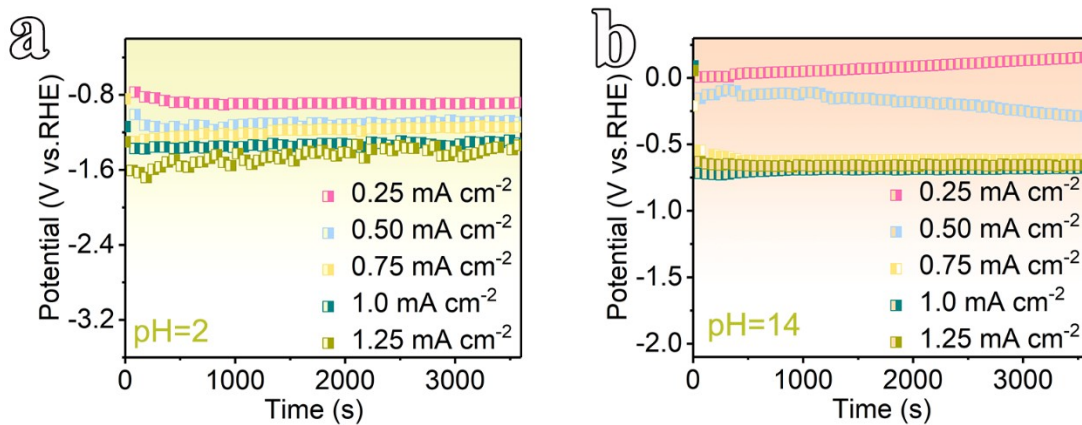
**Supplementary Fig. 35** Calibration curves for  $\text{NH}_4\text{Cl}$  in 1 M KOH solution. (a) UV-vis absorption spectra; (b) the calibration curve.



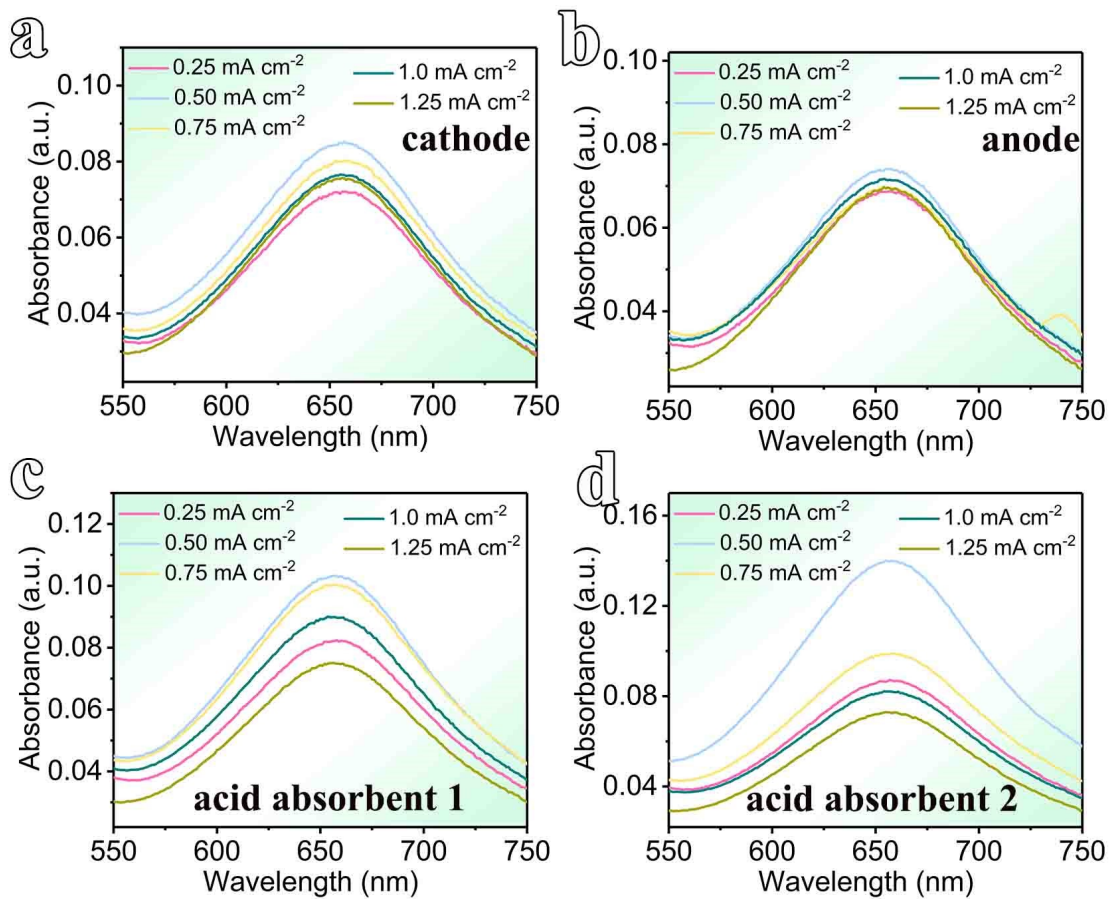
**Supplementary Fig. 36** Calibration curves for  $N_2H_4$  in  $0.05\text{ M } H_2SO_4$  solution. (a) UV-vis absorption spectra; (b) the calibration curve.



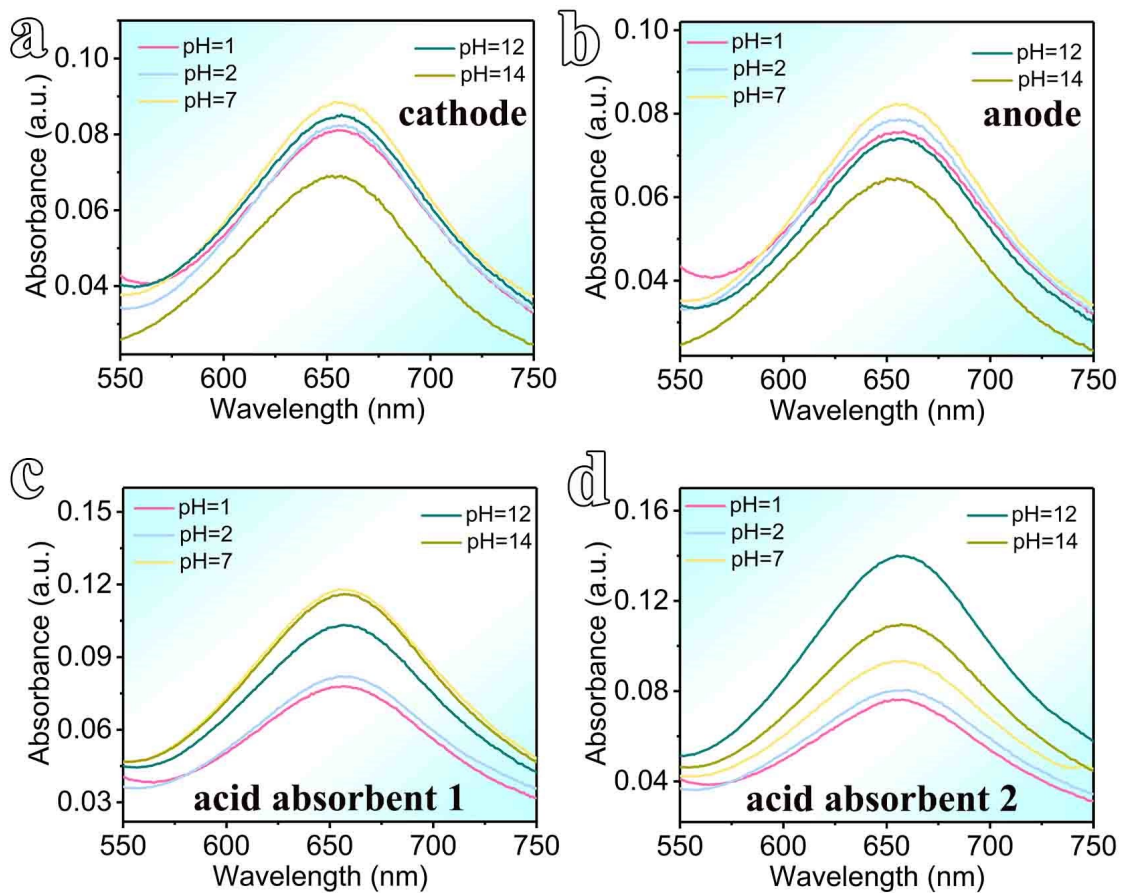
**Supplementary Fig. 37** Calibration curves for N<sub>2</sub>H<sub>4</sub> in 0.1 M Na<sub>2</sub>SO<sub>4</sub> solution. (a) UV-vis absorption spectra; (b) the calibration curve.



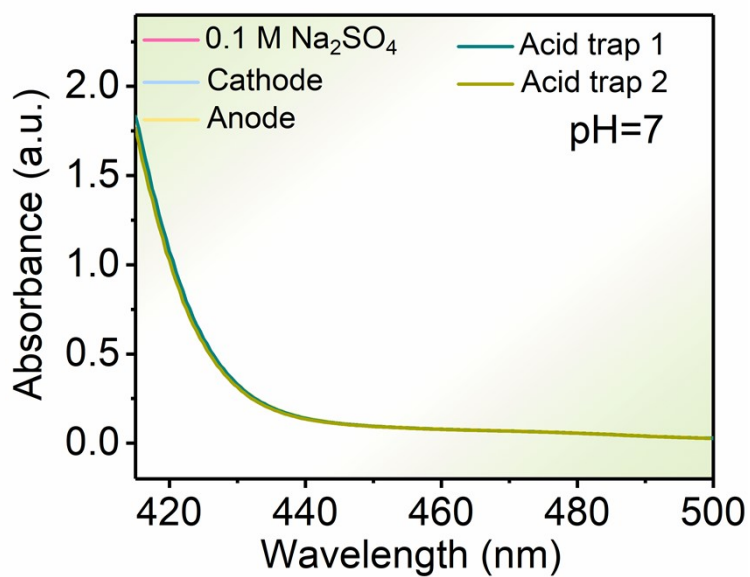
**Supplementary Fig. 38** The chronoamperometric curves of 2D In-MOF nanosheets in different electrolytes: (a) 0.005 M H<sub>2</sub>SO<sub>4</sub> (pH=2). (b) 1 M KOH (pH=14).



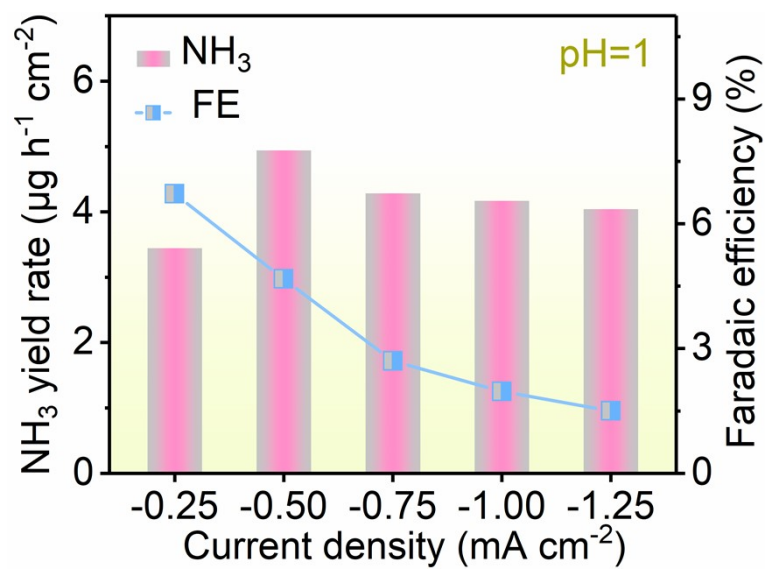
**Supplementary Fig. 39** The UV-vis absorption spectra for NRR catalyzed by 2D In-MOF nanosheets at different current densities for 1 hr in N<sub>2</sub>-saturated 0.01 M KOH (pH=12) solution.



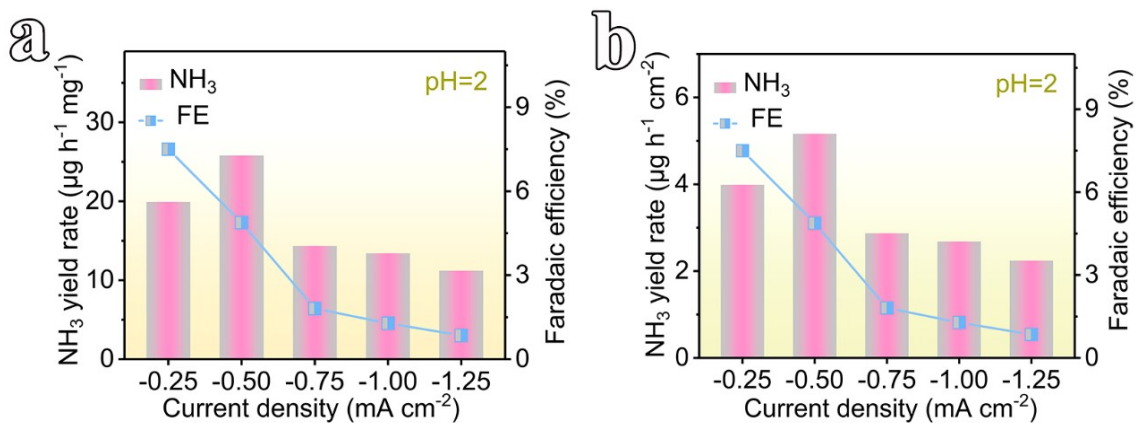
**Supplementary Fig. 40** The UV-vis absorption spectra for NRR catalyzed by 2D In-MOF nanosheets in different electrolytes at  $0.5 \text{ mA cm}^{-2}$  for 1 hr.



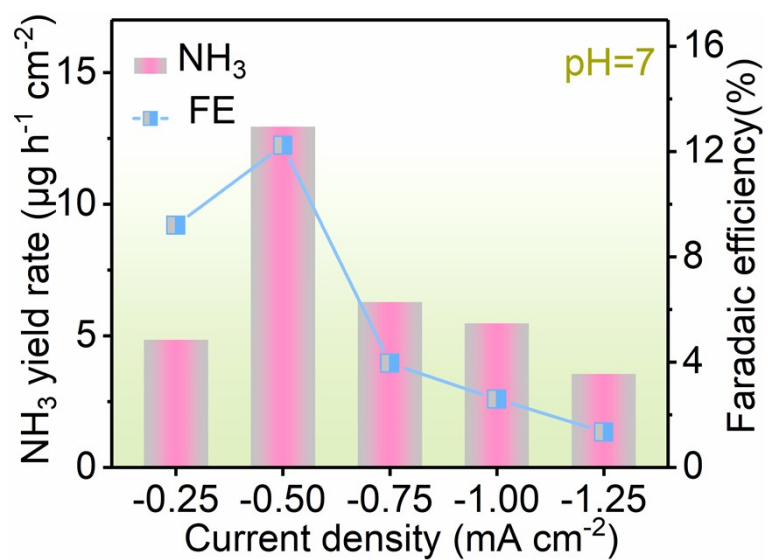
**Supplementary Fig. 41** Watt-Chrisp method to determine the possible hydrazine byproduct using 2D In-MOF as the NRR electrocatalyst at  $0.5 \text{ mA cm}^{-2}$  for 1 hr electrolysis in  $\text{N}_2$ -saturated  $0.1 \text{ M Na}_2\text{SO}_4$  solution. All UV-vis curves show no peaks at  $455 \text{ nm}$ , indicating that no hydrazine is produced during the reaction process.



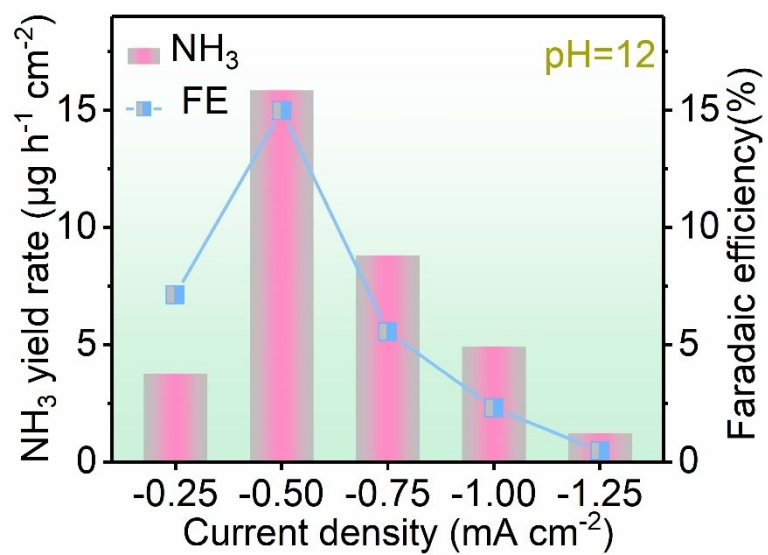
**Supplementary Fig. 42** NH<sub>3</sub> yield rates (per geometric area) and FEs of NRR promoted by 2D In-MOF nanosheets at different applied current densities in 0.05 M H<sub>2</sub>SO<sub>4</sub> electrolyte.



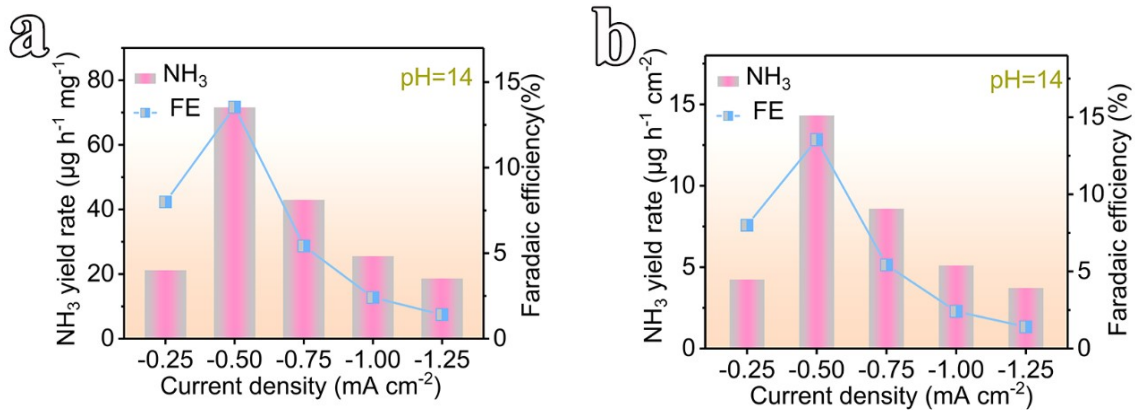
**Supplementary Fig. 43** NH<sub>3</sub> yield rates and FEs of NRR promoted by 2D In-MOF nanosheets at different applied current densities in 0.005 M H<sub>2</sub>SO<sub>4</sub> electrolyte (pH=2): (a) per unit mass; (b) per unit geometric area.



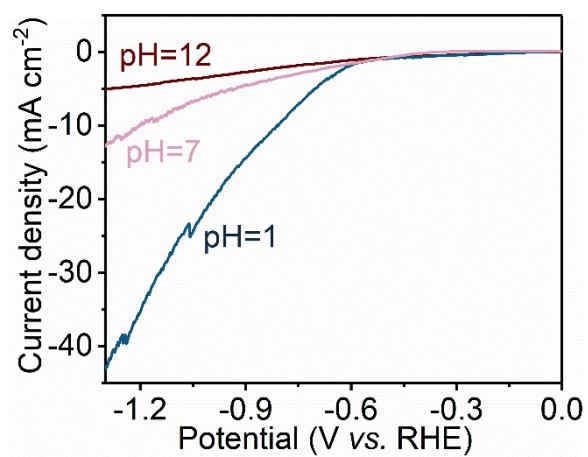
**Supplementary Fig. 44** NH<sub>3</sub> yield rates per geometric areas and FEs of NRR promoted by 2D In-MOF nanosheets at different applied current densities in 0.1 M Na<sub>2</sub>SO<sub>4</sub> electrolyte (pH=7).



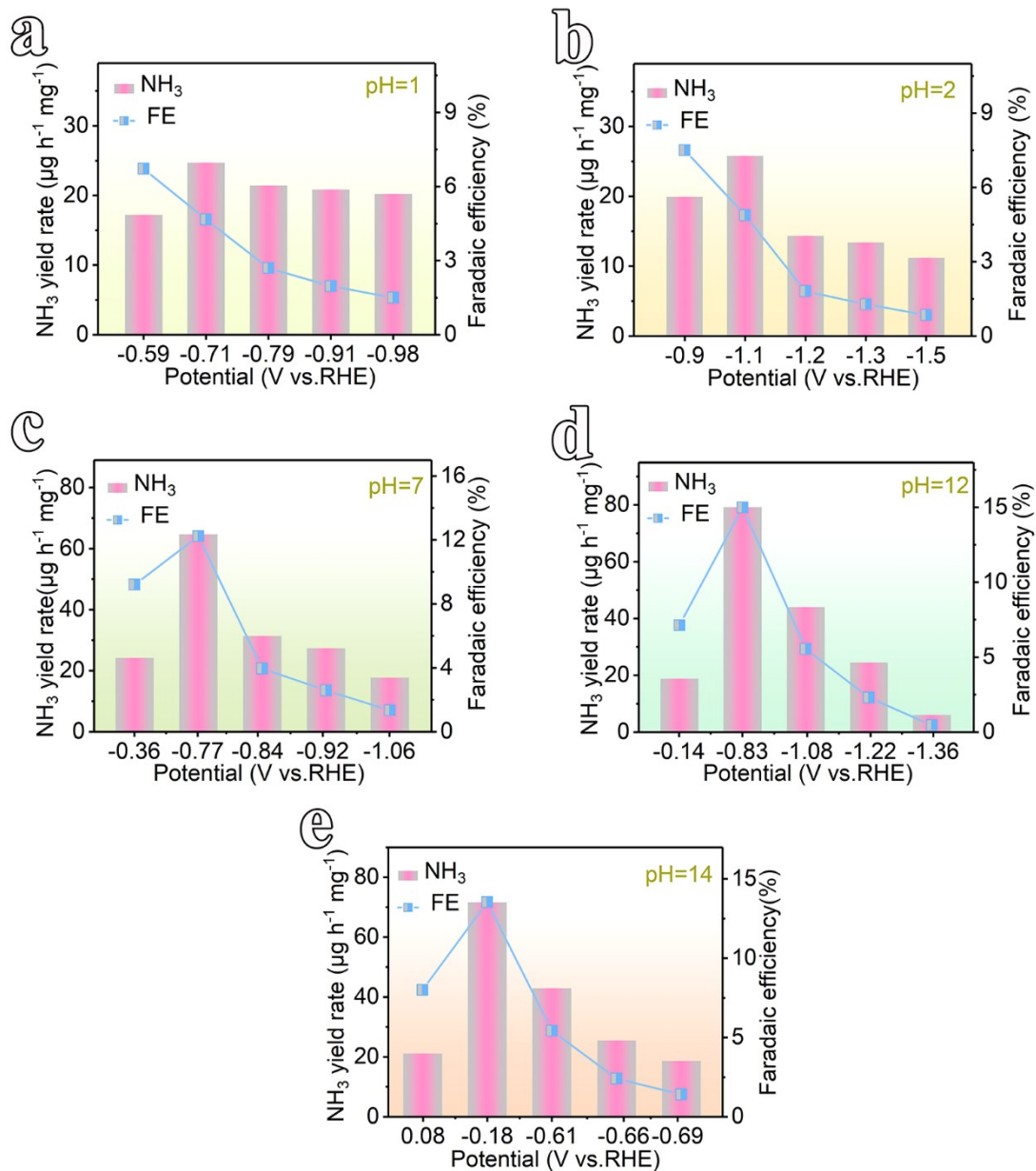
**Supplementary Fig. 45** NH<sub>3</sub> yield rates per geometric areas and FEs of NRR promoted by 2D In-MOF nanosheets at different applied current densities in 0.01 M KOH electrolyte (pH=12).



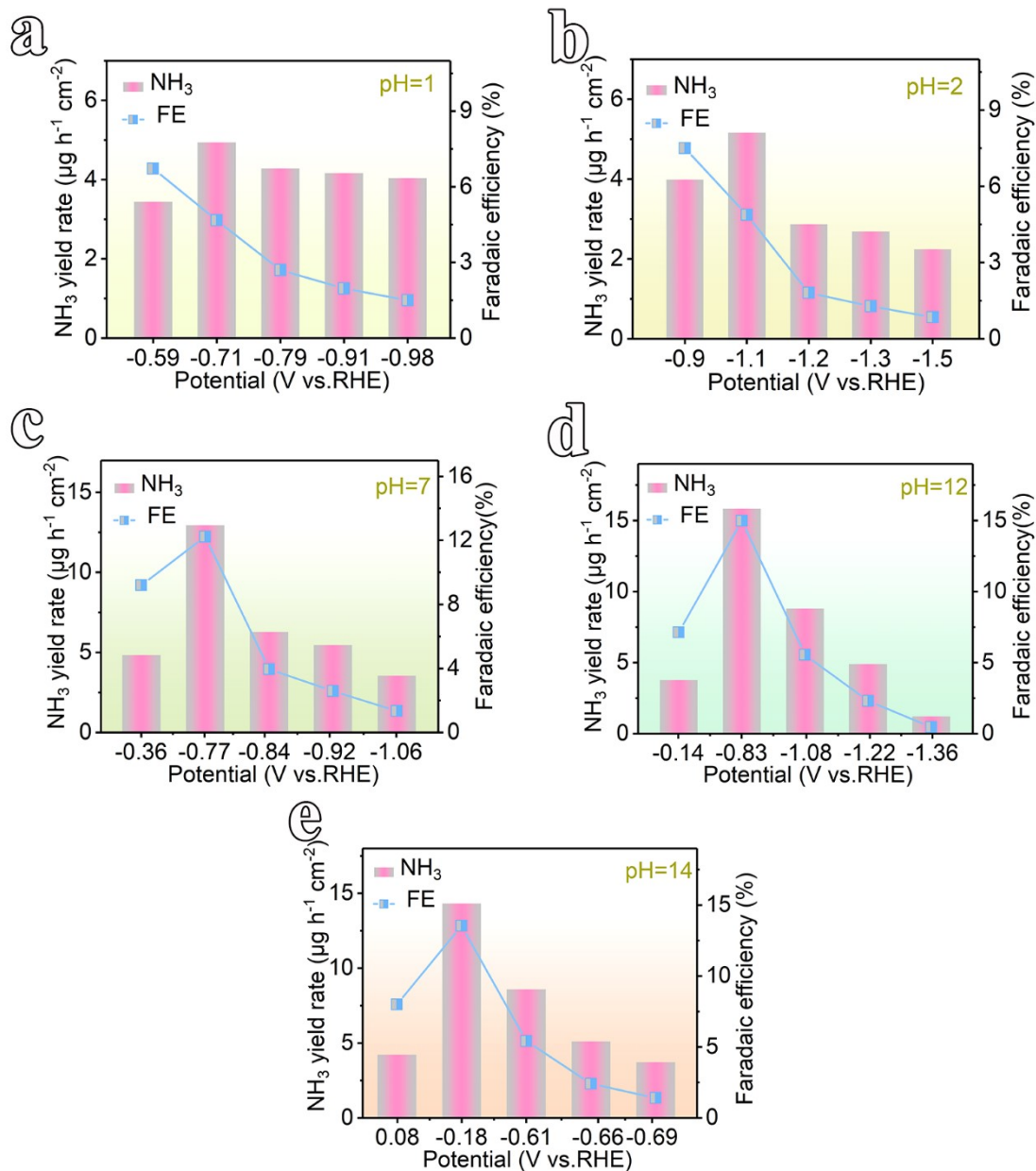
**Supplementary Fig. 46** NH<sub>3</sub> yield rates and FEs of NRR promoted by 2D In-MOF nanosheets at different applied currents in 1 M KOH electrolyte (pH=14): (a) per unit mass and (b) per unit geometric area.



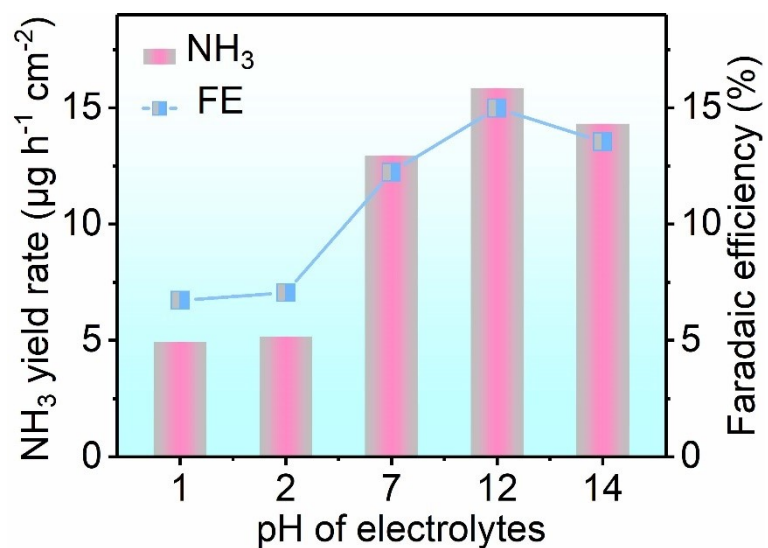
**Supplementary Fig. 47** LSV curves of 2D In-MOF nanosheets for HER with a scan rate of 5 mV s<sup>-1</sup> in Ar-saturated electrolytes with different pH values.



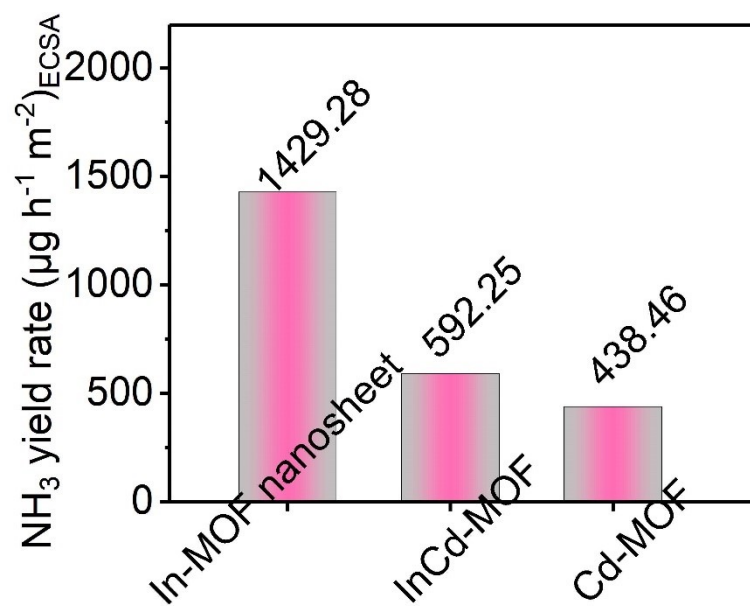
**Supplementary Fig. 48** NH<sub>3</sub> yield rates per unit mass and FEs of NRR promoted by 2D In-MOF nanosheets at different applied potentials in electrolytes with different pH values: (a) pH=1. (b) pH=2. (c) pH=7. (d) pH=12. (e) pH=14.



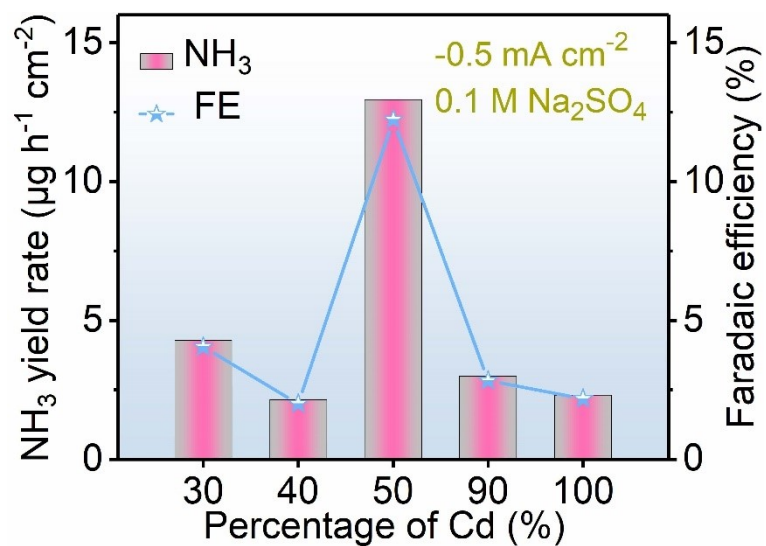
**Supplementary Fig. 49** NH<sub>3</sub> yield rates per geometric areas and FEs of NRR promoted by 2D In-MOF nanosheets at different applied potentials in electrolytes with different pH values: (a) pH=1. (b) pH=2. (c) pH=7. (d) pH=12. (e) pH=14.



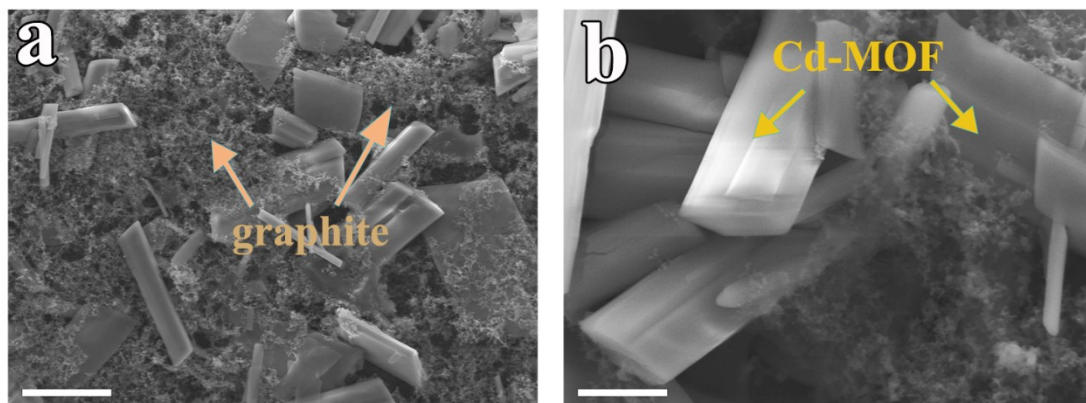
**Supplementary Fig. 50** NH<sub>3</sub> yield rates per geometric areas and FEs of NRR promoted by 2D In-MOF nanosheets at  $-0.5 \text{ mA cm}^{-2}$  in electrolytes with different pH values.



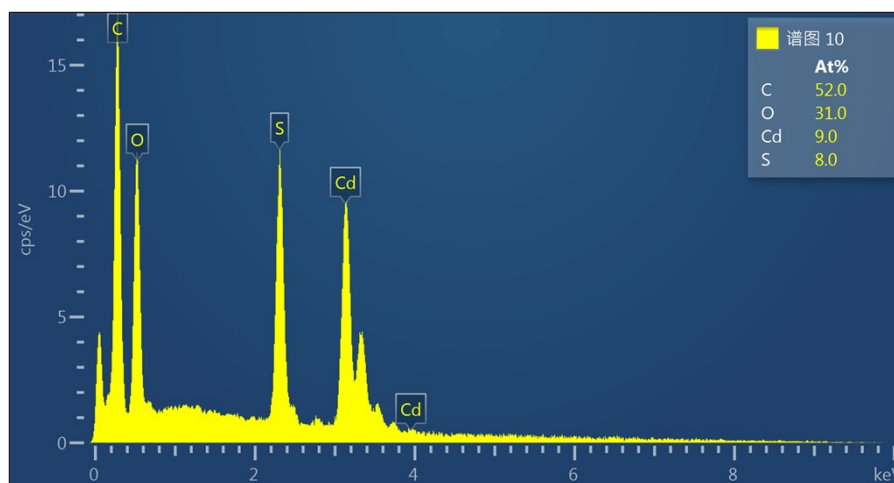
**Supplementary Fig. 51** NH<sub>3</sub> yield rates normalized according to ECSA of NRR promoted by 2D In-MOF nanosheets and other as-prepared materials.



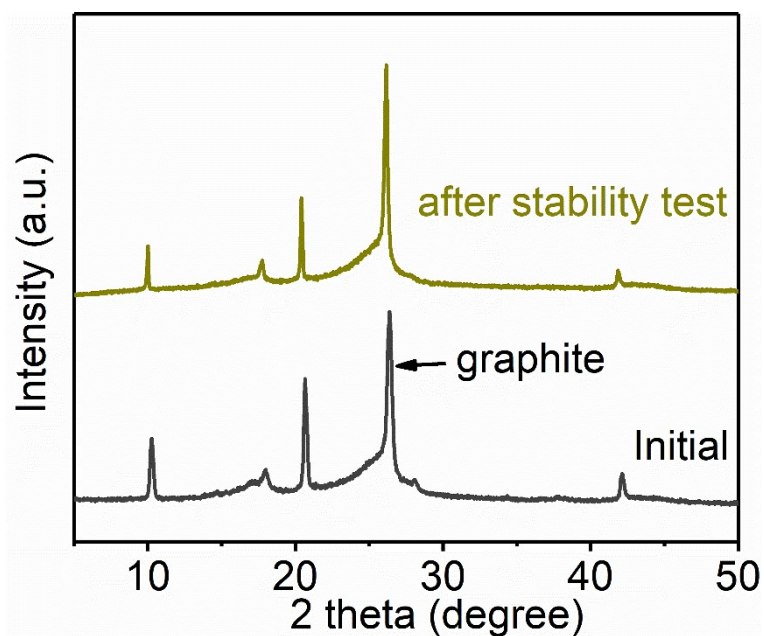
**Supplementary Fig. 52** NH<sub>3</sub> yield rates per geometric area and FEs of In-MOF nanosheets and other control samples synthesized using different amounts of Cd salts at  $-0.5 \text{ mA cm}^{-2}$  in  $0.1 \text{ M Na}_2\text{SO}_4$  electrolyte.



**Supplementary Fig. 53** SEM images of the electrode prepared using Cd-MOF after stability test at  $-0.5 \text{ mA cm}^{-2}$  for 12 hrs (scale bars for a and b are  $1 \mu\text{m}$  and  $500 \text{ nm}$ ).

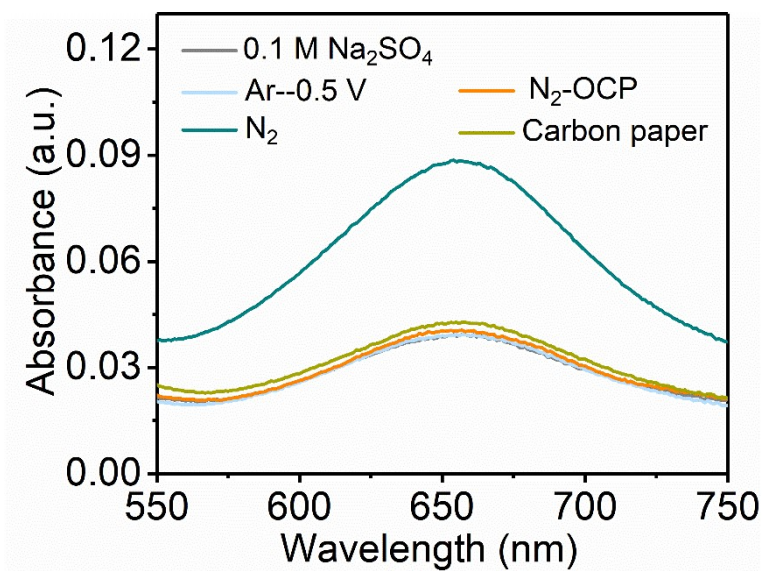


**Supplementary Fig. 54** EDS profile of the electrode prepared using Cd-MOF after stability test in 0.01 M KOH at  $-0.5 \text{ mA cm}^{-2}$  for 12 hrs.

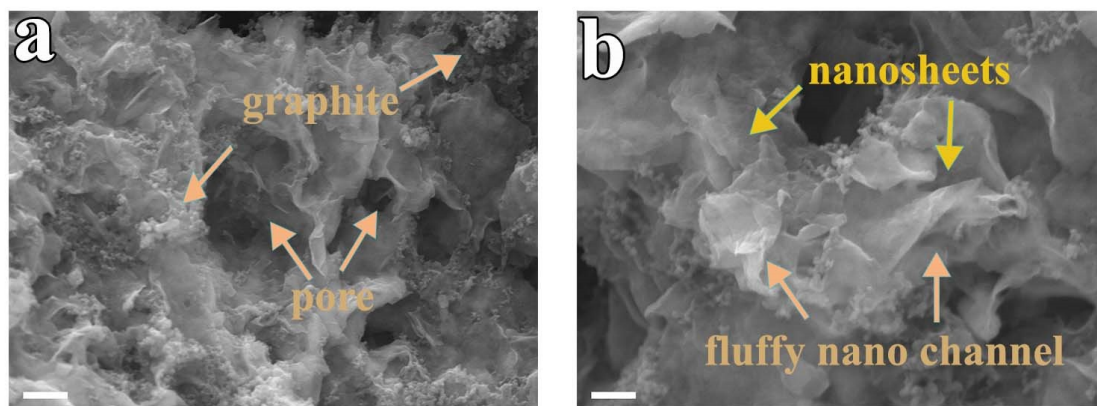


**Supplementary Fig. 55** XRD patterns of electrode prepared using Cd-MOF before and after stability tests at  $-0.5 \text{ mA cm}^{-2}$  for 12 hrs.

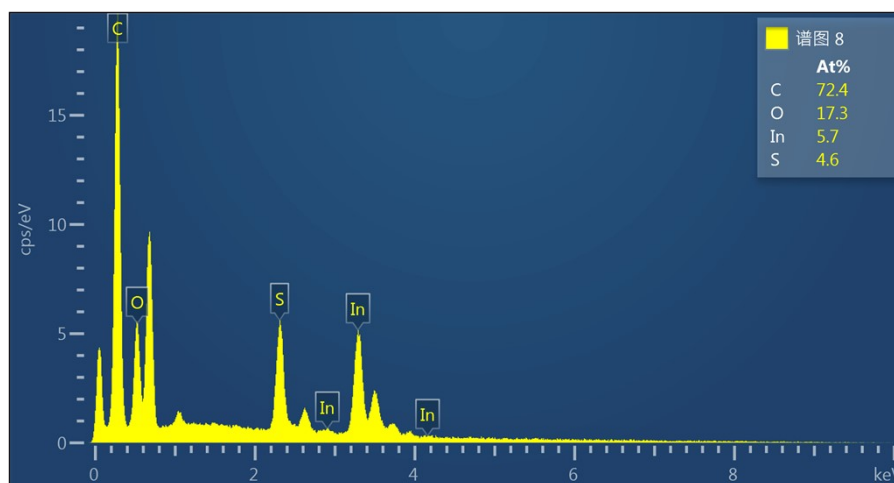
As shown in Supplementary Fig. 52-54, all the analysis shows little change for the electrode after durability test of NRR. Nevertheless,  $\text{NH}_3$  yield and FE of Cd-MOF is far lower than In-MOF nanosheets, which is due to scarce catalytic active sites of Cd-MOFs.



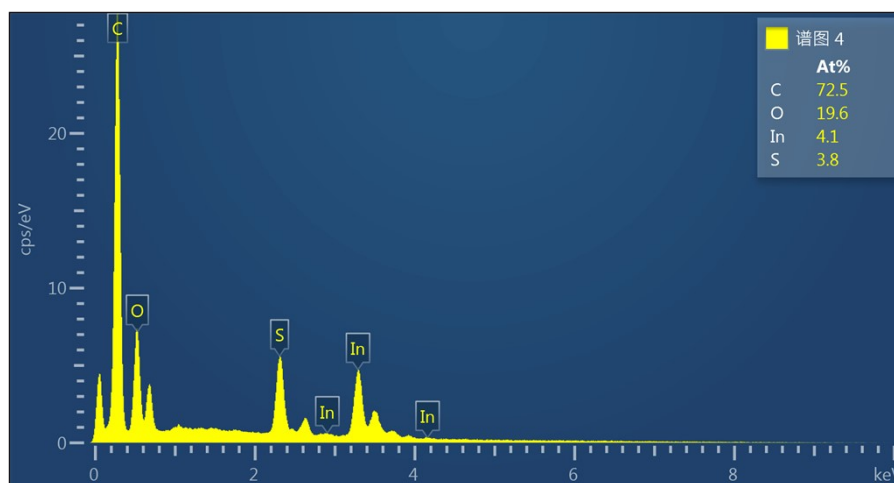
**Supplementary Fig. 56** The UV-vis absorption spectra of test solution collected from NRR operated under different conditions.



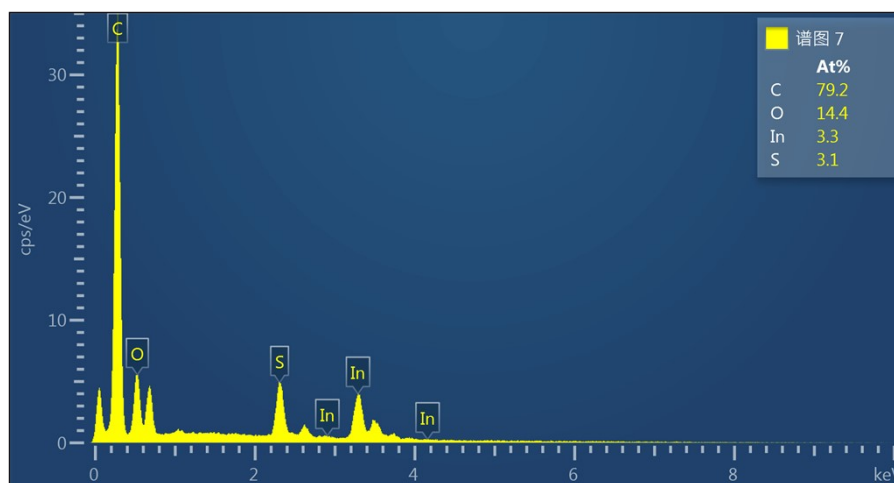
**Supplementary Fig. 57** SEM images of the electrode prepared using 2D In-MOF nanosheets after stability test at  $-0.5 \text{ mA cm}^{-2}$  for 12 hrs (scale bars for a and b are  $1 \mu\text{m}$  and  $500 \text{ nm}$ ).



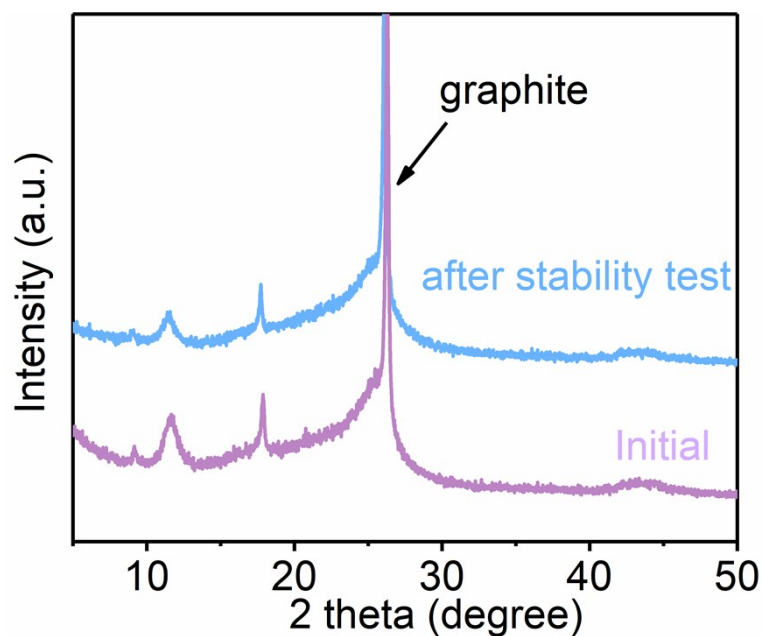
**Supplementary Fig. 58** EDS of the electrode prepared using 2D In-MOF nanosheets after stability test in 0.05 M H<sub>2</sub>SO<sub>4</sub> at -0.5 mA cm<sup>-2</sup> for 12 hrs.



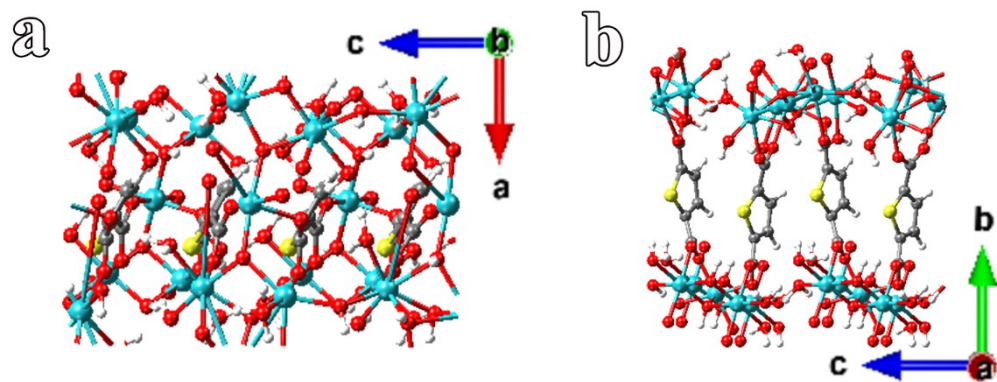
**Supplementary Fig. 59** EDS of the electrode prepared using 2D In-MOF nanosheets after stability test in 0.1 M Na<sub>2</sub>SO<sub>4</sub> at -0.5 mA cm<sup>-2</sup> for 12 hrs.



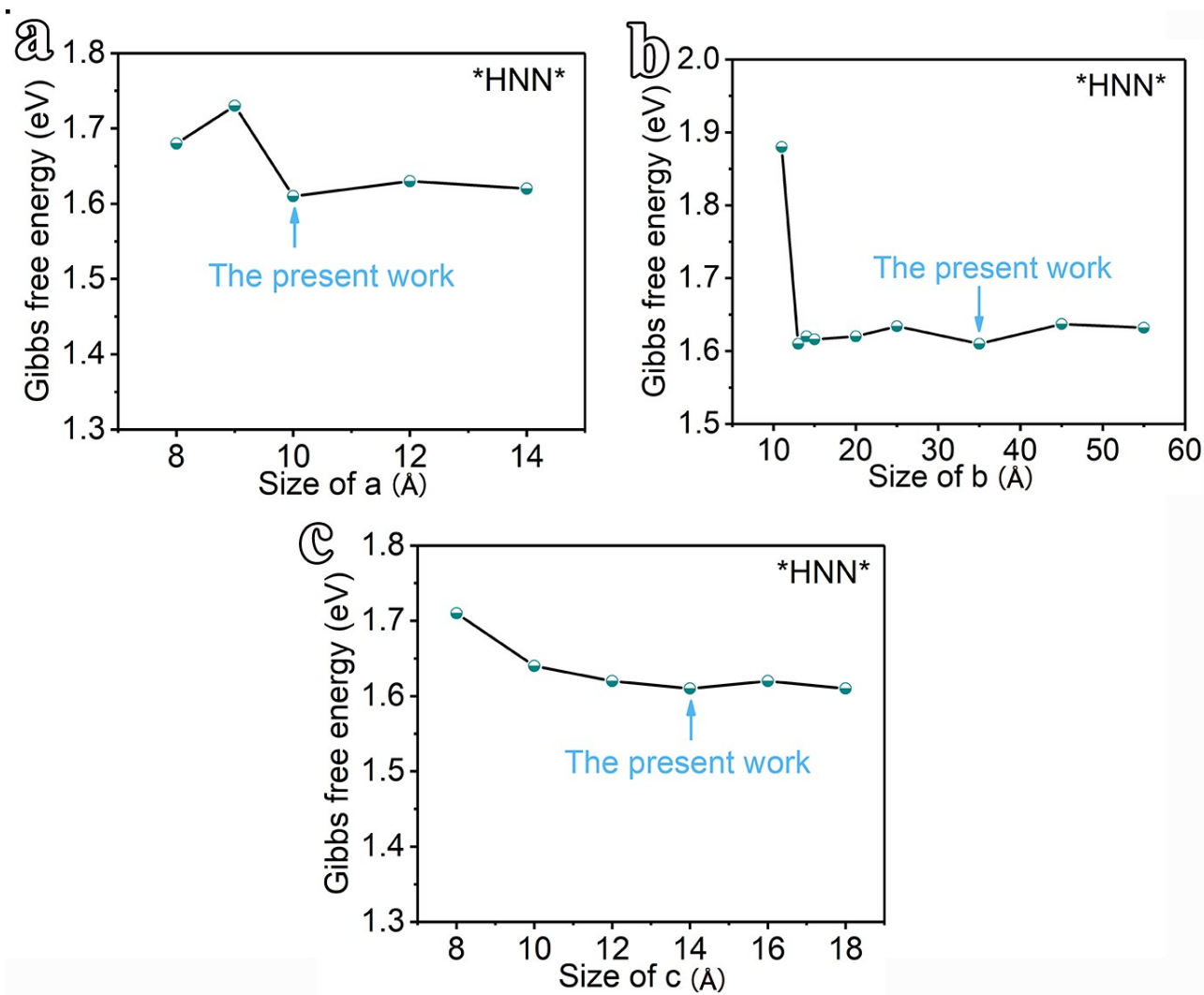
**Supplementary Fig. 60** EDS of the electrode prepared using 2D In-MOF nanosheets after stability test in 0.01 M KOH at  $-0.5 \text{ mA cm}^{-2}$  for 12 hrs.



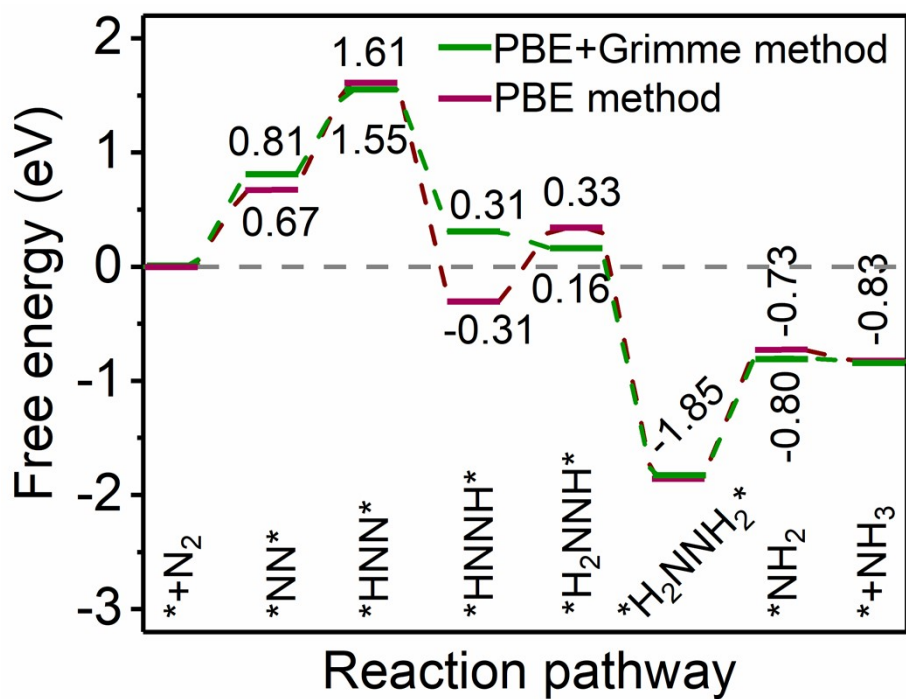
**Supplementary Fig. 61** XRD patterns of electrode prepared using 2D In-MOF nanosheets before and after stability tests at  $-0.5 \text{ mA cm}^{-2}$  for 12 hrs. The characteristic peaks are still present after testing, indicating good structural stability of the electrode. Note that the additional peak for graphite is originated from conductive additives during electrode fabrication.



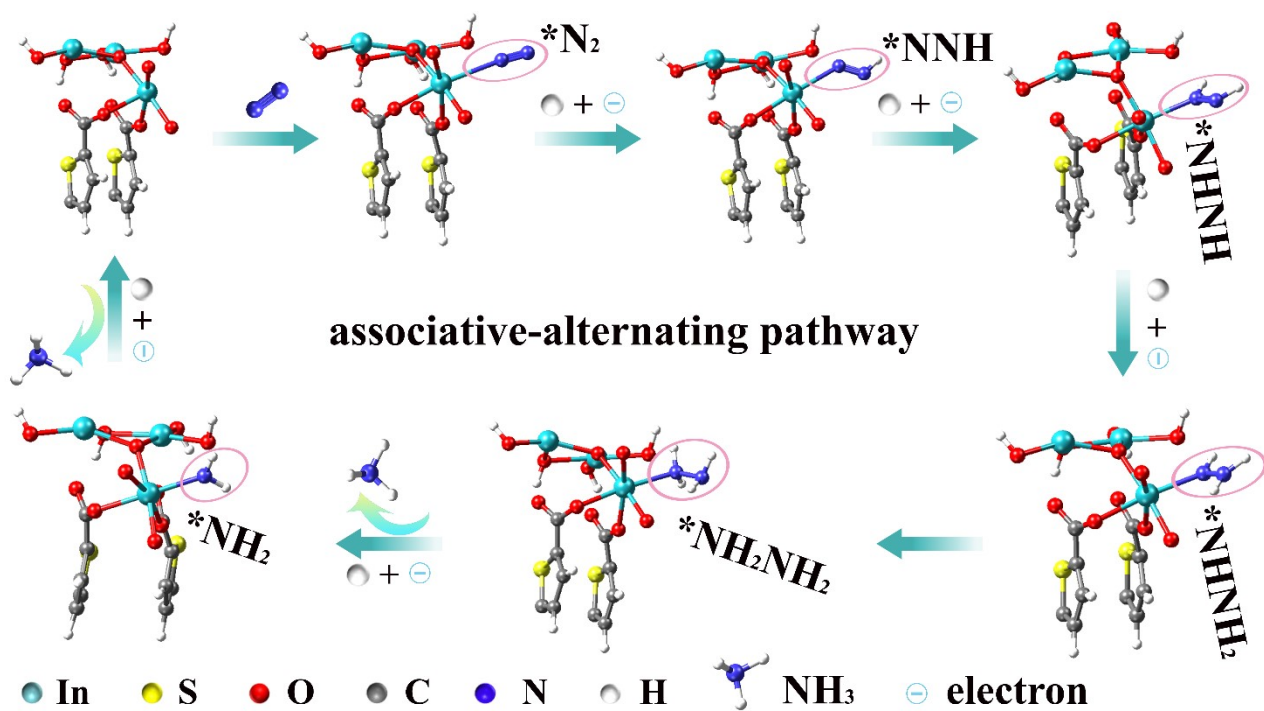
**Supplementary Fig. 62** Optimized lattice structures for In-MOF. Color code: gray, nickel; green, manganese; red, oxygen; yellow, sulfur; white, hydrogen; black, carbon.



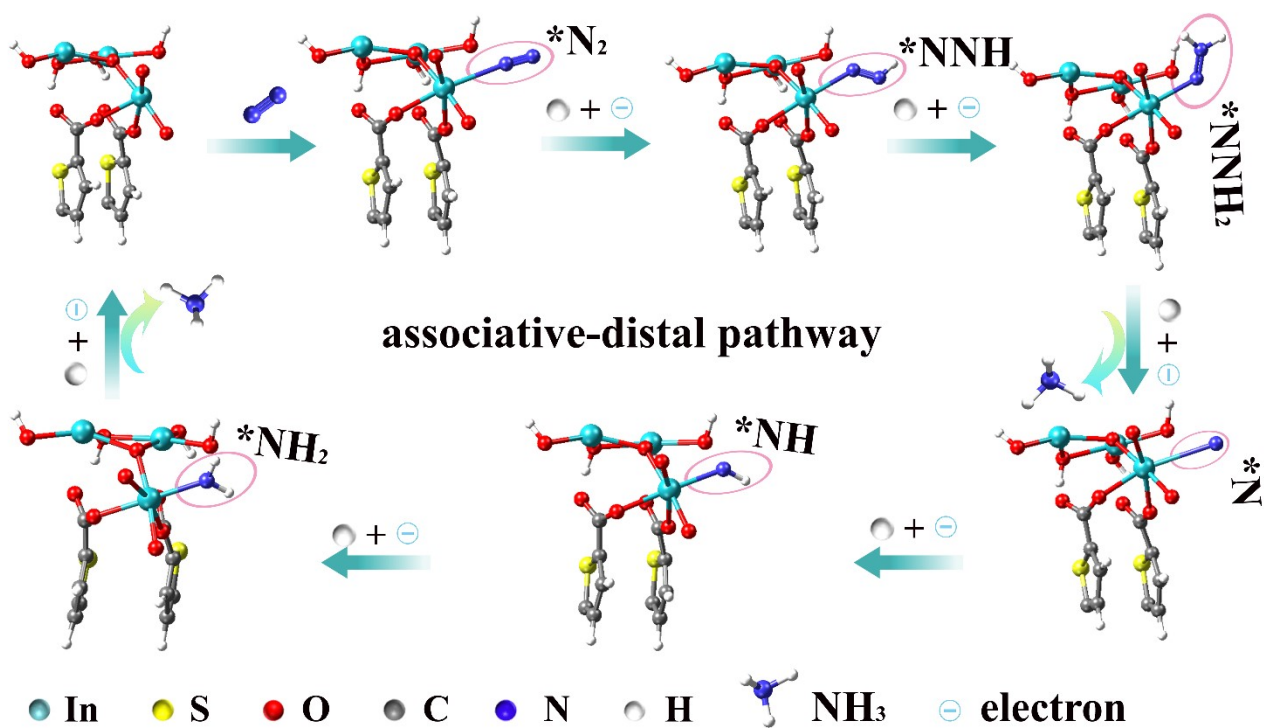
**Supplementary Fig. 63** Changes of Gibbs free energy of \*HNN\* intermediate with the size of crystal box.



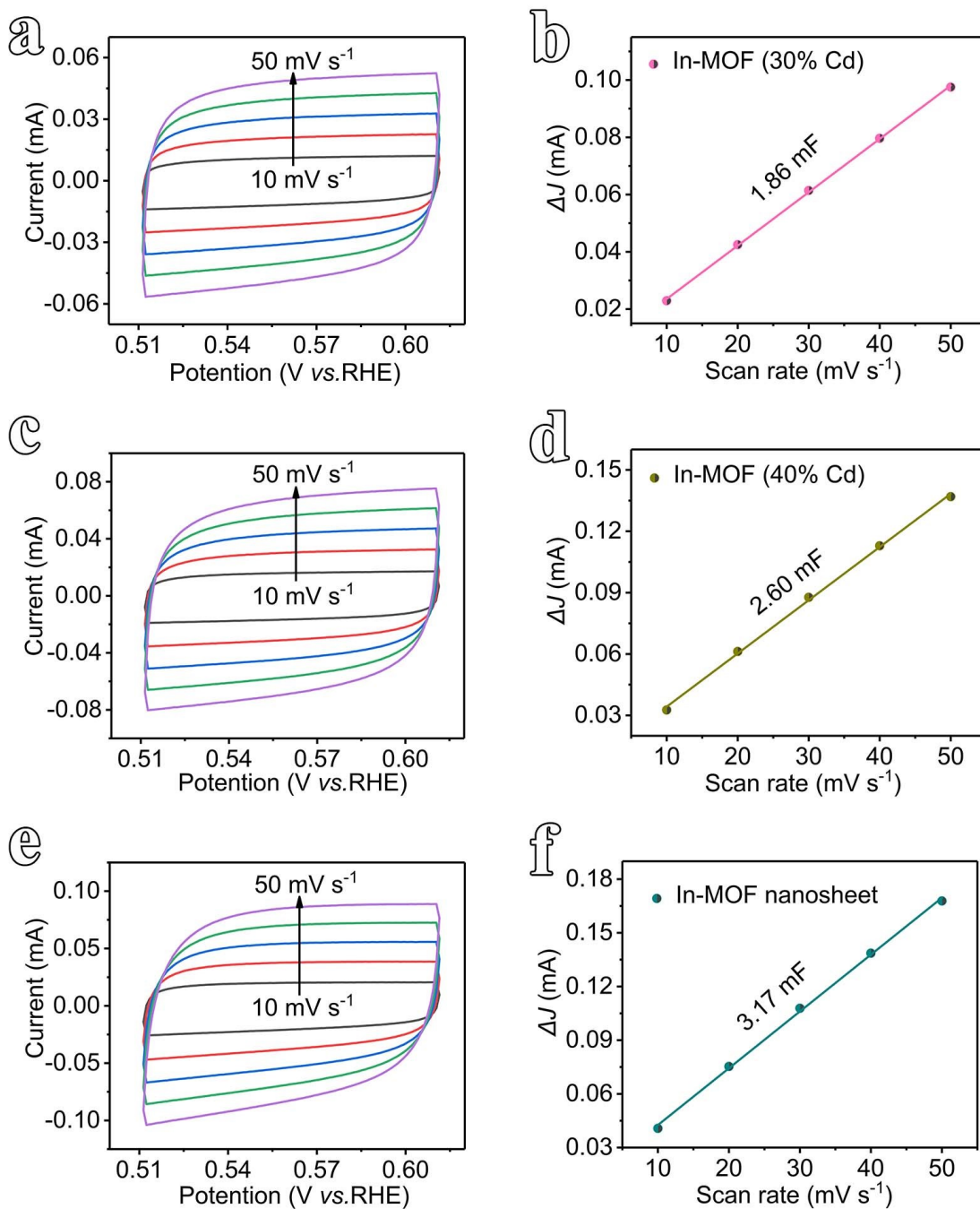
**Supplementary Fig. 64** Free energy of different intermediates for NRR calculated by PBE and PBE-Grimme methods.



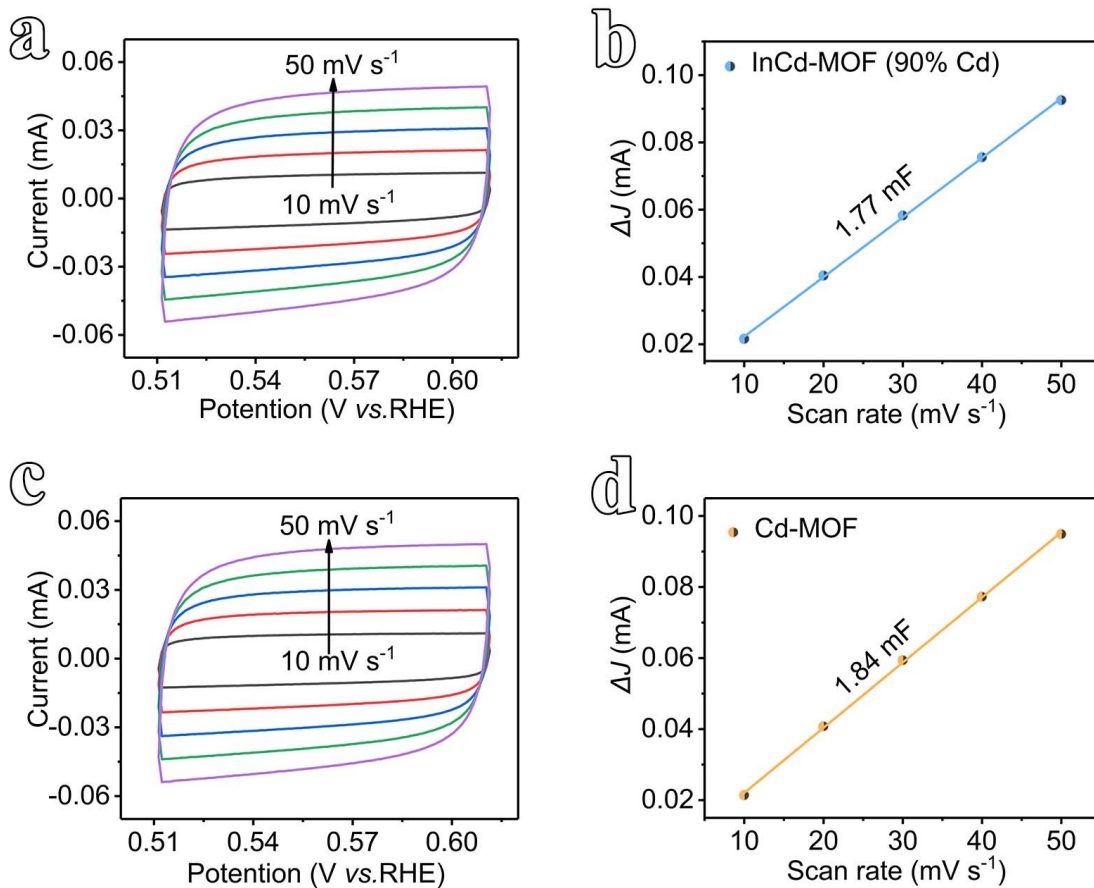
**Supplementary Fig. 65** DFT calculations of possible associative-alternating pathways for NRR promoted by 2D In-MOF nanosheets.



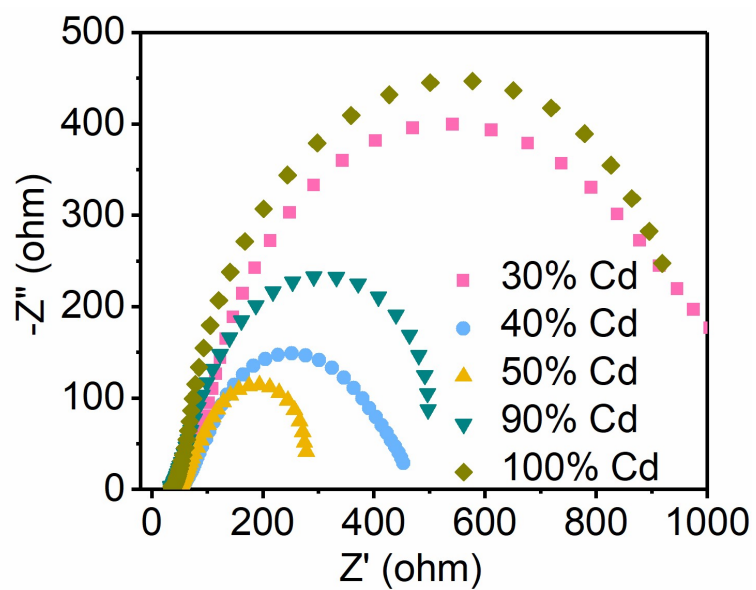
**Supplementary Fig. 66** DFT calculations of possible associative-distal pathways for NRR promoted by 2D In-MOF nanosheets.



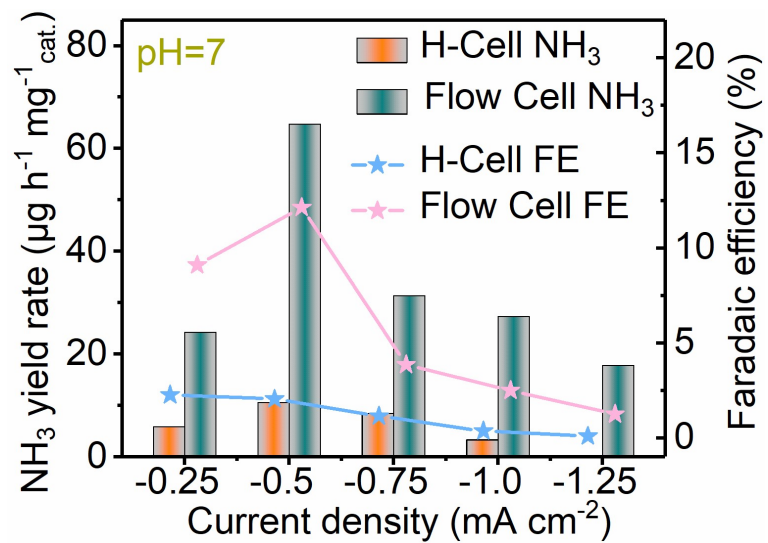
**Supplementary Fig. 67** ECSA data for 2D In-MOF nanosheets and other control samples, In MOF (30%) and (40%). (a, c, e) the corresponding CVs measured at different scan rates from 10 to 50 mV s<sup>-1</sup> in a potential region of 0.5-0.6 V (vs. RHE); (b, d, f) the  $\Delta J$  ( $J_a - J_c$ ) at 0.55 V (vs. RHE) plotted vs. scan rates, where their slopes ( $2C_{dl}$ ) are used to calculate ECSA.



**Supplementary Fig. 68** ECSA data for In-MOF control samples: InCd-MOF (90% Cd) and Cd-MOF (100% Cd). (a, c) the corresponding CVs measured at different scan rates from 10 to 50 mV s<sup>-1</sup> in a potential region of 0.5-0.6 V (vs. RHE); (b, d) the  $\Delta J$  ( $J_a - J_c$ ) at 0.55 V (vs. RHE) plotted vs. scan rates, where the slopes ( $2C_{dl}$ ) are used to calculate the ECSA. According to Supplementary Fig. 54 and 55, ECSA values of In-MOF nanosheet (90.57 cm<sup>2</sup>) are higher than those of In-MOF (30% Cd, 53.14 cm<sup>2</sup>), In-MOF (40% Cd, 74.29 cm<sup>2</sup>), InCd-MOF (90% Cd, 50.57 cm<sup>2</sup>), and Cd-MOF (100% Cd, 52.57 cm<sup>2</sup>).



**Supplementary Fig. 69** EIS plots of 2D In-MOF nanosheets and other control samples in 0.1 M  $\text{Na}_2\text{SO}_4$  electrolyte.



**Supplementary Fig. 70** The optimal NH<sub>3</sub> yield rates and FEs of 2D In-MOF nanosheets in a flow-cell compared to a H-cell at -0.55 V (vs. RHE) in 0.1 M Na<sub>2</sub>SO<sub>4</sub> electrolyte.

**Supplementary Table 1.** Detection of In, Cd, S, O and C contents in In-MOF by ICP-MS, XPS and EDS analysis.

	pH	Content (At.%)				
		In	Cd	S	O	C
<b>ICP-MS</b>		35.5448	0.0286	-	-	-
<b>XPS</b>		6.77	0	7.02	32.64	53.56
<b>EDS</b>	pH=1	7.0	0	6.4	33.7	52.9
<b>EDS after stability test</b>		5.7	0	4.6	17.3	72.4
<b>ICP-MS</b>		35.6006	0.0522	-	-	-
<b>XPS</b>		6.77	0	7.46	35.88	49.89
<b>EDS</b>	pH=7	6.3	0	6.0	36.1	51.6
<b>EDS after stability test</b>		4.1	0	3.8	19.6	72.5
<b>ICP-MS</b>		35.5221	0.0277			
<b>XPS</b>	pH=12	6.40	0	6.88	31.50	55.22
<b>EDS</b>		6.4	0	5.9	31.0	56.7

---

**EDS after  
stability  
test**

3.3

0

3.1

14.4

79.2

---

**Supplementary Table 2.** The Brunauer-Emmett-Teller (BET) surface areas and pore volumes of In-MOF nanosheets treated in solutions with different pH values.

<b>pH values</b>	<b>BET surface area (m<sup>2</sup> g<sup>-1</sup>)</b>	<b>BJH volume of pores ( cm<sup>3</sup> g<sup>-1</sup>)</b>
<b>pH=1</b>	60.31	0.45
<b>pH=7</b>	61.62	0.46
<b>pH=12</b>	62.63	0.48

**Supplementary Table 3.** Comparison of NRR activity of 2D In-MOF nanosheets with several recently reported electrocatalysts.

Catalyst	Electrolyte	Working current (mA cm <sup>-2</sup> )	NH <sub>3</sub> yield	FE	Reference
<b>In-MOF nanosheets</b>	<b>0.01 M KOH</b>	<b>-0.5</b>	<b>79.20 μg h<sup>-1</sup> mg<sup>-1</sup></b>	<b>14.98%</b>	<b>This work</b>
MIL-100 (Al)	0.1 M KOH	-0.25	10.6 μg h <sup>-1</sup> mg <sup>-1</sup>	22.6%	5
2D Co <sub>3</sub> Fe-MOF	0.1 M KOH	<-0.1	8.97 μg h <sup>-1</sup> mg <sup>-1</sup>	25.64%	6
HKUST-1 (Cu- BTC)	0.1 M Na <sub>2</sub> SO <sub>4</sub>	~-0.9	46.64 μg h <sup>-1</sup> mg <sup>-1</sup>	2.45%	7
NiFe-MOF	0.1 M NaHCO <sub>3</sub>	-0.2	9.3 μg h <sup>-1</sup> mg <sup>-1</sup>	11.5%	8
Few-layer black phosphorus nanosheets	0.01 M HCl	-0.45	31.37 μg h <sup>-1</sup> mg <sup>-1</sup>	5.07%	9
BND <sub>2</sub> -NC	0.05 M H <sub>2</sub> SO <sub>4</sub> +0.2 M Li <sub>2</sub> SO <sub>4</sub>	-0.13	19.1 μg h <sup>-1</sup> cm <sup>-2</sup>	21.2%	10
Cl-RGO	0.05 M H <sub>2</sub> SO <sub>4</sub>	-0.25	70.9 μg h <sup>-1</sup> mg <sup>-1</sup>	5.97%	11
NiTe{001}	0.1 M HCl	-0.2	33.34 μg h <sup>-1</sup> mg <sup>-1</sup>	17.38%	12
3D amorphous	0.1 M Na <sub>2</sub> SO <sub>4</sub>	-0.25	17.5 μg h <sup>-1</sup>	13.8%	13

BiNi			mg <sup>-1</sup>		
Defect-rich Bi	0.1 M Na <sub>2</sub> SO <sub>4</sub>	-0.08	5.43 μg h <sup>-1</sup> mg <sup>-1</sup>	11.68%	14
NiFe-nanomesh array	0.1 M Na <sub>2</sub> SO <sub>4</sub>	<-0.2	16.89 μg h <sup>-1</sup> mg <sup>-1</sup>	12.50%	15
Fex-COF/NC	0.1 M KOH	-0.09	12.53 μg h <sup>-1</sup> mg <sup>-1</sup>	45.43%	16

## Supplementary References

1. Y. Luo, G.-F. Chen, L. Ding, X. Chen, L.-X. Ding and H. Wang, *Joule*, 2019, **3**, 279-289.
2. J. P. Perdew, K. Burke and M. Ernzerhof, *Phys. Rev. Lett.*, 1996, **77**, 3865-3868.
3. J. G. Kresse and J. Furthmüller, *Com. Mater. Sci.*, 1996, **6**, 15-50.
4. J. G. Kresse and J. Furthmüller, *Phys. Rev. B* 1996, **54**, 11169-11186.
5. Y. Fu, K. Li, M. Batmunkh, H. Yu, S. Donne, B. Jia and T. Ma, *ACS Appl. Mater. Inter.*, 2020, **12**, 44830-44839.
6. W. Li, W. Fang, C. Wu, K. N. Dinh, H. Ren, L. Zhao, C. Liu and Q. Yan, *J. Mater. Chem. A*, 2020, **8**, 3658-3666.
7. Y. Cao, P. Li, T. Wu, M. Liu and Y. Zhang, *Chem. Asian. J.*, 2020, **15**, 1272-1276.
8. J. Duan, Y. Sun, S. Chen, X. Chen and C. Zhao, *J. Mater. Chem. A*, 2020, **8**, 18810-18815.
9. L. Zhang, L. Ding, G. Chen, X. Yang and H. Wang, *Angew. Chem. Int. Ed.*, 2019, **58**, 2612-2616.
10. B. Liu, Y. Zheng, H.-Q. Peng, B. Ji, Y. Yang, Y. Tang, C.-S. Lee and W. Zhang, *ACS Energy Lett.*, 2020, **5**, 2590-2596.
11. P. Huang, Z. Cheng, L. Zeng, J. Yu, L. Tan, P. Mohapatra, L. S. Fan and Y. Zhu, *ACS Catal.*, 2020, **10**, 14928-14935.
12. M. Yuan, Q. Li, J. Zhang, J. Wu, T. Zhao, Z. Liu, L. Zhou, H. He, B. Li and G. Zhang, *Adv. Funct. Mater.*, 2020, **30**, 2004208-2004216.
13. Z. Fang, P. Wu, Y. Qian and G. Yu, *Angew. Chem. Int. Ed.*, 2020, **60**, 4275-4281.
14. Y. Wang, M. M. Shi, D. Bao, F. L. Meng, Q. Zhang, Y. T. Zhou, K. H. Liu, Y. Zhang, J. Z. Wang, Z. W. Chen, D. P. Liu, Z. Jiang, M. Luo, L. Gu, Q. H. Zhang, X. Z. Cao, Y. Yao, M. H. Shao, Y. Zhang, X. B. Zhang, J. G. Chen, J. M. Yan and Q. Jiang, *Angew. Chem. Int. Ed.*, 2019, **58**, 9464-9469.
15. Y. Sun, T. Jiang, J. Duan, L. Jiang, X. Hu, H. Zhao, J. Zhu, S. Chen and X. Wang, *ACS Catal.*, 2020, **10**, 11371-11379.
16. S. Liu, M. Wang, T. Qian, H. Ji, J. Liu and C. Yan, *Nat. Commun.*, 2019, **10**, 3898.